Frequency varying rheology-based fluid–structure-interactions waves in liquid-filled visco-elastic pipes

A. Bayle, F. Rein, F. Plouraboué

Abstract

This contribution proposes a new rheology-based model for water-hammer wave propagation in visco-elastic pipes. Using a long wavelength analysis and a generalized frequency-dependent Hooke-law for the stress/strain relation, the pressure/longitudinal stress coupled wave system is derived. In this general framework, a visco-elastic Fluid-Structure Interaction (FSI) four equations model is derived by having four visco-elastic kernels associated with the non-local time response of the visco-elastic solid. The explicit dependence of these kernels with the material creep function and the pipe dimension is found. Considering a general linear visco-elastic rheology, the four visco-elastic kernels, and the corresponding creep function are explicitly derived in frequency and time-domain versus four visco-elastic parameters. For a given set of boundary conditions, a general analytical solution for the pressure/stress water hammer wave is obtained in frequency domain. The model's predictions are successfully compared with experimental measurements as well as with other models adjusted to the same experimental data set by calibrating the model's parameter. The proposed model can be used in many other contexts with the specific ability to distinguish the intrinsic visco-elastic rheology from the considered pipe geometry and boundary conditions.

Highlights

Frequency varying rheology-based fluid-structure-interactions waves in liquid-filled visco-elastic pipes.

A.Bayle, F.Rein, F.Plouraboué

- A fluid-structure-interaction water-hammer model for linear visco-elastic rheology is derived.
- It involves new history-dependent visco-elastic response through time-convolution kernels.
- It does not need Kelvin-Voigt calibrated parameters, but rheological ones.
- The dispersive wave velocity is also obtained explicitly versus rheological parameters.

Frequency varying rheology-based fluid-structure-interactions waves in liquid-filled visco-elastic pipes.

A.Bayle[a], F.Rein[a,b], F.Plouraboué[a]

[a]*Institut de Mécanique des Fluides de Toulouse, IMFT, Université de Toulouse, CNRS, Toulouse, 31400, France*
[b]*Institut de Recherche sur les Phénomène Hors Equilibre, IRPHE, Université d'Aix-Marseille, CNRS, Marseille, 13013, France*

Keywords: visco-elastic rheology, Kelvin-Voigt, water-hammer, creeping-law, fluid-structure-interactions, polymer pipes, dispersive waves

1. Introduction

Pressure waves in visco-elastic tubes is a topic of importance in many hydraulic contexts [1] as well as biomechanical ones [2, 3, 4, 5, 6]. It is known for a long time that when a water-hammer wave propagates into a filled-fluid pipe, the visco-elastic properties of the solid wall drastically modifies the nature and characteristic of its motion. More precisely, the importance of visco-elastic stress-strain response of the pipe wall in the water-hammer waves propagation was first raised by [7]. A few years later some experiments from the same team [8] complemented with a 1D theoretical model [9] confirmed the relevance and interest of these effects on water-hammer waves propagation. As opposed to the situation of a purely elastic solid tube, the wave velocity becomes dispersive when a visco-elastic wall is present [2, 10, 11]. Secondly, not only the wave velocity depends on the considered frequency, but it also acquires an imaginary component associated with visco-elastic dissipation resulting in exponential damping [12, 13, 14, 15]. Such exponential damping is also present in water-hammer wave propagation within elastic filled-fluid pipes but for a very distinct mechanism: the viscous dissipation arises only within the liquid boundary layers [16, 17]. Nevertheless, compared to this viscous damping, the visco-elastic one turns out to be dominant in many configurations, resulting in the filtering of high-frequency bouncing elastic waves. Recently, [18] indeed analysed the energy rates of dissipation in the fluid and the pipe for visco-elastic water-hammer.

Since most aspects of water-hammer wave propagation have been found material dependant, the pioneering studies of [7, 8, 9] inspired many others, following the similar footsteps, combining experimental measurements with one-dimensional two-equations modelling associated with pressure (hydraulic head) and axial velocity coupled propagation coupled with solid creep-functions displaying Kelvin-Voigt behaviour (Cf [19, 13, 14, 20] among others). The applicative interest and the relevance of the topic motivated many further studies whereby one could enrich the Kelvin-Voigt model [21, 22] to better fit with observations. Alternatively, some authors also included both solid visco-elastic damping and fluid one, through time-convolution shear-stress models [23, 24, 25]. Because the modelling relies on many parameters, combined with time-convolution many approaches are possible to match experiments raising a number of questions including wave-speed calibration in visco-elastic pipes [20, 26]. The influence of the visco-elastic stress response has been more recently considered in a Fluid-Structure-Interaction (FSI) context as more extensively discussed in the recent review of [27]. In this context Kelvin-Voigt solid responses of the creep function have also been used in FSI four-equations models [28, 29] in order to improve the relevance of

the modelling. Furthermore, for improving data fitting, a series of Kelvin-Voigt units are often considered [28, 30, 29, 31]. However, in these previous modelling, the creep-function parameters are calibrated [32] not only to describe the visco-elastic properties of the solid but also the considered pipe configuration associated with a specific length, thickness, diameter and boundary conditions. Nevertheless, Kelvin-Voigt units leading to a thermodynamic consistent framework of internal stress-strain theory have recently been proposed in [31] so as to improve their mechanical background.

In this contribution we pursue in this direction with the aim of stepping aside from Kelvin-Voigt models from considering rheology-based visco-elastic modelling of water-hammer propagation within a visco-elastic solid. The aim of this contribution is thus to distinguish and clarify the respective contribution of the visco-elastic response within pressure/stress wave propagation from the considered boundary conditions and pipe configuration. This permits to propose a new rheology-based visco-elastic FSI four equations model which can be used in many configurations (pipe's and boundary conditions) with material dependent only, visco-elastic kernels. The parameters of this model evidently need calibration. One option undertaken in this contribution is to use the existing pressure measurements of the water-hammer wave dynamic for inverse transient analysis of the model's parameter [32, 33]. Another possible option opened by our contribution is to perform the parameter calibration/estimation from rheological measurements of the pipe material. The advantage of such rheology-based parameter calibration is to precisely focus the model estimation independently of the specific configuration at end for water-hammer use (hence not depending on the configuration geometry, pipe supports, flow conditions, boundary conditions, etc...). Whilst the latter is interesting, it is beyond the scope of the present contribution from the lack of existing data. The details of the protocol for this rheological-based parameter calibration are nevertheless presented in Appendix A.

The paper is organised as follows. Section S.2 provides a first overview of notations and considered problems. Using a long wavelength analysis and a generalised frequency-dependent Hooke-law for the stress/strain relation the pressure/longitudinal stress coupled wave system (equivalent to the classical four-equations Fluid-Structure Interaction (FSI) description) is derived in section S.3. The resulting set of equations involves four visco-elastic kernels directly related to the generalised frequency-dependent Hooke-law, the visco-elastic dispersive speed wave being solved as an explicit function of those. Considering specific visco-elastic rheology in S. 4.1, a specific set of boundary conditions in S.4.2, an explicit solution for the resulting visco-elastic FSI is derived in section S.4.2. It is then compared with previously proposed models as well as with experimental observations in section S. 4.5.

2. General considerations concerning visco-elastic material and their FSI waves.

2.1. Physical analysis overview

We consider the axi-symmetric propagation of a pressure/stress wave inside a Newtonian liquid filling a visco-elastic cylindrical tube. The circular visco-elastic-walled pipe tube has a thickness e, an inner radius R_0, and a length L_0 whilst its density is set constant equal to ρ_s. The solid has both an elastic Poisson's modulus ν_e and Young modulus E_e. The fluid is assumed isothermal and inviscid of constant density ρ_f, bulk modulus $\mathcal{K}_f$ and crossed by an acoustic overpressure P^*, the elastic wave speed of which is set to c_p^e ([34, 35])

$$c_p^e = \frac{c_0}{\sqrt{1+\chi_e \mathcal{C}^2}}, \qquad c_0 = \sqrt{\frac{\mathcal{K}_f}{\rho_f}}, \qquad \chi_e = \frac{2\mathcal{K}_f}{\alpha E_e \mathcal{C}^2}\left(\frac{2(1-\nu_e^2)}{2+\alpha} + \alpha\,(1+\nu_e)\right), \qquad \mathcal{C} = \frac{c_0}{c_p^e}, \tag{1}$$

which depends on the dimensionless pipe thickness $\alpha = e/R_0$ and the bulk fluid acoustic velocity c_0. From this definition of χ_e, one can find a trivial but important relation $\mathcal{C}^2 = 1 + \chi_e \mathcal{C}^2$ or alternatively $\mathcal{C} = \sqrt{1/(1-\chi_e)}$. The pulse speed wave is also given by $c_p^e = c_0/\mathcal{C} = c_0\sqrt{(1-\chi_e)}$ from definition of $\mathcal{C}$ in (1)) which is also important to consider for the simplification of the visco-elastic model provided in Appendix B.

In the solid, a deformation occurs due to the propagation of the acoustic fluid overpressure waves, the displacement of which is

$$\boldsymbol{\xi}^* = \xi^* \mathbf{e}_r + \zeta^* \mathbf{e}_z. \tag{2}$$

where (ξ^*, ζ^*) are respectively the radial and axial displacements, whereas $(\mathbf{e}_r, \mathbf{e}_z)$ are the cylindrical coordinates unit vectors in the radial and axial directions. These deformations are associated with solid stress tensor

$$\boldsymbol{\sigma}_s^* = \begin{pmatrix} \sigma_{rr}^* & 0 & \sigma_{rz}^* \\ 0 & \sigma_{\theta\theta}^* & 0 \\ \sigma_{rz}^* & 0 & \sigma_{zz}^* \end{pmatrix}. \tag{3}$$

The wave advective time-scale L/c_p^e is chosen as a reference for the physical time t, whilst the length of the pipe L and radius R_0 as a reference length-scale in the longitudinal and radial direction (r, z), respectively, so that dimensionless time and coordinates are set

$$\tau = \frac{c_p^e}{L} t, \quad Z = \frac{z}{L}, \quad R = \frac{r}{R_0}, \quad \text{and} \quad \epsilon = \frac{R_0}{L}, \tag{4}$$

where we also introduce the tube aspect-ratio being a small parameter $\epsilon \ll 1$ as one key feature of the problem on which a long wavelength approximation is based. In the following the Fourier transform of a causal function $f^*(t)$, i.e. $f^*(t) = 0$ if $t < 0$, is denoted $\tilde{f}(\omega^*)$ from

$$\tilde{f}^*(\omega^*) = \int_{-\infty}^{\infty} f^*(t) e^{-i\omega^* t} dt \equiv \int_0^{\infty} f^*(t) e^{-i\omega^* t} dt, \tag{5}$$

with associated pulsation ω^*. When a dimensionless system is regarded, the pulsation ω^* has to be substituted by the dimensionless pulsation ω such that

$$\omega^* = \frac{c_p^e}{L} \omega. \tag{6}$$

2.2. Visco-elastic solid rheology

2.2.1. General linear dynamical rheological model

In Fourier space, the dimensional form of the 3D solid rheology is a frequency-dependent generalized Hooke-law [3]

$$\tilde{\boldsymbol{\sigma}}_s^* = \tilde{\lambda}_s^*(\omega^*)\, \mathrm{Tr}\,(\tilde{\boldsymbol{\epsilon}}_s^*)\, \mathbf{I} + 2\tilde{\mu}_s^*(\omega^*) \tilde{\boldsymbol{\epsilon}}_s^* \quad \text{, and,} \quad \tilde{\boldsymbol{\epsilon}}_s^* = \frac{1}{2}\left(\boldsymbol{\nabla} \tilde{\boldsymbol{\xi}}^* + \boldsymbol{\nabla}^T \tilde{\boldsymbol{\xi}}^* \right). \tag{7}$$

where Tr is trace, $\tilde{\lambda}_s^*, \tilde{\mu}_s^*$ are the generalized Lamé coefficients, dependent on pulsation ω^*. These coefficients provide the respective spherical and deviatoric response of the elastic deformation, depending on the considered pulsation ω^*, i.e. the response to oscillating compression and oscillating

shear stress. From them, one can deduce the generalized Poisson and Young coefficients

$$2\tilde{\nu}_s^*(\omega^*) = \frac{\tilde{\lambda}_s^*(\omega^*)}{\tilde{\lambda}_s^*(\omega^*) + \tilde{\mu}_s^*(\omega^*)}, \quad \tilde{E}_s^*(\omega^*) = \frac{\tilde{\mu}_s^*(\omega^*)\left[3\tilde{\lambda}_s(\omega^*) + 2\tilde{\mu}_s^*(\omega^*)\right]}{\tilde{\lambda}_s^*(\omega^*) + \tilde{\mu}_s^*(\omega^*)}. \tag{8}$$

Subscript s stands thereafter for solid generalized physical fields or quantities. Also, from these relations one can deduce the reverse Lamé coefficients versus Poisson and Young coefficients

$$\tilde{\lambda}_s^*(\omega^*) = \frac{\tilde{\nu}_s^*(\omega^*)\tilde{E}_s^*(\omega^*)}{(1+\tilde{\nu}_s^*(\omega^*))(1-2\tilde{\nu}_s^*(\omega^*))}, \qquad \tilde{\mu}_s^*(\omega^*) = \frac{\tilde{E}_s^*(\omega^*)}{2(1+\tilde{\nu}_s^*(\omega^*))}. \tag{9}$$

This notation embeds both elastic and visco-elastic contributions. In this general context, one needs to specify the functional dependence of generalized Lamé coefficients on pulsation ω^*. Nevertheless, it is not easy to deduce them from experimental measurements as discussed in Appendix A. This is the reason for considering explicit rheological constitutive laws as later on considered in S.4.

2.3. Dimensionless parameters and physical fields scaling

The general Lamé-Clapeyron rheological parameters (8)-(9) are scaled to their elastic counterparts [3]

$$2\nu_e = \frac{\lambda_e}{\lambda_e + \mu_e} \text{ , and, } E_e = \frac{\mu_e\,(3\lambda_e + 2\mu_e)}{\lambda_e + \mu_e}, \tag{10}$$

so that

$$\tilde{\nu}_s^*(\omega^*) = \nu_e\tilde{\nu}_s(\omega), \qquad \tilde{E}_s^*(\omega^*) = E_e\tilde{E}_s(\omega), \tag{11}$$

$$\tilde{\lambda}_s^*(\omega^*) = \lambda_e\tilde{\lambda}_s(\omega), \qquad \tilde{\mu}_s^*(\omega^*) = \mu_e\tilde{\mu}_s(\omega). \tag{12}$$

The couple $\left(\tilde{\nu}_s, \tilde{E}_s\right)$ then corresponds to the re-scaled Poisson and Young visco-elastic modulus, respectively. The solid axial visco-elastic and elastic propagating wave speeds are furthermore set up regarding these dimensionless functions [1]

$$\tilde{c}_s^*(\omega^*) = \sqrt{\frac{\tilde{E}^*(\omega^*)}{\rho_s}} = c_s^e\sqrt{\tilde{E}_s(\omega)} \text{ , with } c_s^e = \sqrt{\frac{E_e}{\rho_s}}, \tag{13}$$

so that their dimensionless ratios to c_p^e of are

$$\mathcal{C}_s^e = \frac{c_s^e}{c_p^e} \text{ , and } \tilde{\mathcal{C}}_s(\omega) = \mathcal{C}_s^e\sqrt{\tilde{E}_s(\omega)}. \tag{14}$$

Four dimensionless Cauchy numbers are associated with the solid elastic and visco-elastic responses to the acoustic pulse pressure one [36]

$$\mathcal{C}_{\mu_e} = \frac{\rho_f c_p^{e2}}{\mu_e}, \qquad \mathcal{C}_{\lambda_e} = \frac{\rho_f c_p^{e2}}{\lambda_e}, \tag{15}$$

$$\tilde{\mathcal{C}}_{\mu_s}(\omega) = \frac{\rho_f c_p^{e2}}{\mu_e\tilde{\mu}_s(\omega)} \equiv \frac{\mathcal{C}_{\mu_e}}{\tilde{\mu}_s(\omega)}, \qquad \tilde{\mathcal{C}}_{\lambda_s}(\omega) = \frac{\rho_f c_p^{e2}}{\lambda_e\tilde{\lambda}_s(\omega)} \equiv \frac{\mathcal{C}_{\lambda_e}}{\tilde{\lambda}_s(\omega)}. \tag{16}$$

Leading to the dimensionless parametrisation of $\tilde{\lambda}_s^*(\omega^*)$ and $\tilde{\mu}_s^*(\omega^*)$

$$\tilde{\lambda}_s(\omega) = \frac{\mathcal{C}_{\lambda_e}}{\tilde{\mathcal{C}}_{\lambda_s}(\omega)} \qquad\qquad \tilde{\mu}_s(\omega) = \frac{\mathcal{C}_{\mu_e}}{\tilde{\mathcal{C}}_{\lambda_s}(\omega)}, \tag{17}$$

and finally, the fluid-solid density ratio is introduced

$$\mathcal{D} = \frac{\rho_f}{\rho_s}. \tag{18}$$

The reference longitudinal fluid velocity is chosen has W_0. From Joukowsky's theory, [37, 38] a reference pressure $\rho_f c_p^e W_0$ is built. This Joukowsky reference pressure is also chosen as reference stresses in the fluid and the solid, so that

$$\mathbf{W}^* = W_0 W \cdot \mathbf{e}_z, \tag{19}$$

$$P^* = \rho_f c_p^e W_0 P. \tag{20}$$

$$[\sigma_{rr}, \sigma_{\theta\theta}, \sigma_{zz}, \sigma_{rz}]^* = \rho_f c_p^e W_0 \left[\sigma_{rr}, \sigma_{\theta\theta}, \sigma_{zz}, \epsilon\sigma_{rz}\right]. \tag{21}$$

Finally, it has been shown in [35] that the solid displacements are related to fluid typical velocity because of kinematic boundary conditions to be applied at the fluid/solid interface. From choosing L/c_p^e as a reference time it results in the appearance of the dimensionless ratio $W_0/c_p^e \equiv \mathcal{M}$ defined as the Mach number, in the solid displacement $\boldsymbol{\xi}^*$ (2) scaling, so that

$$\boldsymbol{\xi}^* = \alpha R_0 \mathcal{M} \left(\xi \mathbf{e}_r + \frac{\zeta}{\epsilon}\mathbf{e}_z\right), \tag{22}$$

3. Dimensionless governing equations

3.1. Solid's equations

In dimensionless form, frequency domain, in cylindrical coordinates (4), the visco-elastic governing equation (7) using (17) reads

$$\tilde{\sigma}_{rr} = \alpha \left[\frac{2}{\tilde{\mathcal{C}}_{\mu_s}(\omega)} + \frac{1}{\tilde{\mathcal{C}}_{\lambda_s}(\omega)}\right] \partial_R \tilde{\xi} + \frac{\alpha}{\tilde{\mathcal{C}}_{\lambda_s}(\omega)} \left[\partial_Z \tilde{\zeta} + \frac{\tilde{\xi}}{R}\right], \tag{23}$$

$$\tilde{\sigma}_{\theta\theta} = \alpha \left[\frac{2}{\tilde{\mathcal{C}}_{\mu_s}(\omega)} + \frac{1}{\tilde{\mathcal{C}}_{\lambda_s}(\omega)}\right] \frac{\tilde{\xi}}{R} + \frac{\alpha}{\tilde{\mathcal{C}}_{\lambda_s}(\omega)} \left[\partial_Z \tilde{\zeta} + \partial_R \tilde{\xi}\right], \tag{24}$$

$$\tilde{\sigma}_{zz} = \alpha \left[\frac{2}{\tilde{\mathcal{C}}_{\mu_s}(\omega)} + \frac{1}{\tilde{\mathcal{C}}_{\lambda_s}(\omega)}\right] \partial_Z \tilde{\zeta} + \frac{\alpha}{\tilde{\mathcal{C}}_{\lambda_s}(\omega)} \frac{\partial_R}{R} \left(R\tilde{\xi}\right), \tag{25}$$

$$\epsilon^2 \frac{\tilde{\mathcal{C}}_{\mu_s}(\omega)}{\alpha} \tilde{\sigma}_{rz} = \partial_R \tilde{\zeta} + \epsilon^2 \partial_Z \tilde{\xi}, \tag{26}$$

where it takes the form of a generalised frequency-dependent Hooke-law (form the linearity of the visco-elastic rheological model (59)). The advantage of these dimensionless forms is to show that some terms are small as they involve the small parameter $\epsilon \ll 1$ [39, 40, 41, 34, 35]. The

dimensionless form of Lamé-Clapeyron equations in frequency domain are [42]

$$-\epsilon^2\left(\omega^2\tilde{\xi}+\partial_Z\tilde{\sigma}_{rz}\right)=\frac{\partial_R}{R}\left(R\tilde{\sigma}_{rr}\right)-\frac{\tilde{\sigma}_{\theta\theta}}{R}, \tag{27}$$

$$-\frac{\alpha}{\mathcal{D}}\omega^2\tilde{\zeta}=\partial_Z\tilde{\sigma}_{zz}+\frac{\partial_R}{R}\left(R\tilde{\sigma}_{rz}\right). \tag{28}$$

Inserting the visco-elastic rheology (23)-(26) into the dimensionless Lamé-Clapeyron equations (27)-(28) leads to the solid dynamical governing equations

$$-\epsilon^2\left(\omega^2+\frac{\mathcal{D}}{\tilde{\mathcal{C}}_{\mu_s}(\omega)}\partial_Z^2\right)\tilde{\xi} = \mathcal{D}\frac{2\tilde{\mathcal{C}}_{\lambda_s}(\omega)+\tilde{\mathcal{C}}_{\mu_s}(\omega)}{\tilde{\mathcal{C}}_{\mu_s}(\omega)\tilde{\mathcal{C}}_{\lambda_s}(\omega)}\partial_R\left(\frac{\partial_R}{R}\left(R\tilde{\xi}\right)\right)+\mathcal{D}\frac{\tilde{\mathcal{C}}_{\mu_s}(\omega)+\tilde{\mathcal{C}}_{\lambda_s}(\omega)}{\tilde{\mathcal{C}}_{\mu_s}(\omega)\tilde{\mathcal{C}}_{\lambda_s}(\omega)}\partial_R\partial_Z\tilde{\zeta}, \tag{29}$$

$$-\epsilon^2\left(\omega^2+\mathcal{D}\frac{2\tilde{\mathcal{C}}_{\lambda_s}(\omega)+\tilde{\mathcal{C}}_{\mu_s}(\omega)}{\tilde{\mathcal{C}}_{\mu_s}(\omega)\tilde{\mathcal{C}}_{\lambda_s}(\omega)}\partial_Z^2\right)\tilde{\zeta} = \frac{\mathcal{D}}{\tilde{\mathcal{C}}_{\mu_s}(\omega)}\frac{\partial_R}{R}\left(R\partial_R\right)\tilde{\zeta}+\epsilon^2\mathcal{D}\frac{\tilde{\mathcal{C}}_{\mu_s}(\omega)+\tilde{\mathcal{C}}_{\lambda_s}(\omega)}{\tilde{\mathcal{C}}_{\mu_s}(\omega)\tilde{\mathcal{C}}_{\lambda_s}(\omega)}\partial_Z\left(\frac{\partial_R}{R}\left(R\tilde{\xi}\right)\right) \tag{30}$$

3.2. Fluid equations

In the fluid region, the dimensionless low-Mach, long-wavelength mass conservation and momentum balance lead to the following outer/core region fluid equations [32, 34, 35]

$$\partial_\tau P+\mathcal{C}^2\partial_Z W = -2\alpha\mathcal{C}^2\partial_\tau\xi\big|_{R=1}, \tag{31}$$

$$\partial_\tau W = -\partial_Z P. \tag{32}$$

From the r.h.s of (31) and the long-wavelength approximation, continuity relations of the radial velocity at the wall is automatically satisfied. Moving to the frequency domain gives

$$i\omega\tilde{P}+\mathcal{C}^2\partial_Z\tilde{W} = -2i\alpha\omega\mathcal{C}^2\tilde{\xi}\big|_{R=1}, \tag{33}$$

$$i\omega\tilde{W} = -\partial_Z\tilde{P}. \tag{34}$$

3.3. Fluid/solid interface boundary conditions

Ignoring external constraints applying to the solid radial direction (supposing a zero external normal stress), and using definition of $\tilde{\sigma}_{rr}$ in (23), the continuity of the normal and tangential stress as well as axial velocity reads (Cf [35] for more details)

$$\tilde{\sigma}_{rr}=-\tilde{P}\ \text{, at}\ \ R=1 \qquad\qquad \tilde{\sigma}_{rr}=0\ \text{, at}\ \ R=1+\alpha \tag{35}$$

$$\tilde{\sigma}_{rz}=0\ \text{, at}\ \ R=1 \qquad\qquad \tilde{\sigma}_{rz}=0\ \text{, at}\ \ R=1+\alpha \tag{36}$$

Note that, for dimensionless radial distance r, since the dimensionless thickness of the pipe is α, the outer wall is reached as $R=1+\alpha$.

$$\tilde{w}=i\alpha\omega\tilde{\zeta}\ \text{, at,}\ \ R=1. \tag{37}$$

3.4. FSI four-equations dimensionless visco-elastic problem derivation

From the combination of the fluid, solid and the fluid-solid interface governing equations, a set of four coupled hyperbolic equations system is obtained upon $(\tilde{P},\tilde{W},\tilde{\sigma}_{zz},\tilde{\zeta})$. Its complete

derivation is provided in Appendix B and achieves as follows [34, 28, 35]

$$
\begin{aligned}
i\omega\tilde{P}+\partial_Z\tilde{W}-2i\omega\alpha\nu_e\partial_Z\tilde{\zeta} &= -i\omega\chi_e\tilde{\mathcal{I}}_P^F\tilde{P}+\frac{2\mathcal{D}\nu_e}{\mathcal{C}_s^{e2}}i\omega\tilde{\mathcal{I}}_\sigma^F\tilde{\sigma}_{zz}, && (38)\\
i\omega\tilde{W} &= -\partial_Z\tilde{P} && (39)\\
i\omega\tilde{\sigma}_{zz}-\frac{2\nu_e}{\alpha(2+\alpha)}i\omega\tilde{P}-i\omega\frac{\alpha\mathcal{C}_s^{e2}}{\mathcal{D}}\partial_Z\tilde{\zeta} &= -i\omega\tilde{\mathcal{I}}_\sigma^S\tilde{\sigma}_{zz}+\frac{2\nu_e}{\alpha(2+\alpha)}i\omega\tilde{\mathcal{I}}_P^S\tilde{P}, && (40)\\
\frac{\alpha}{\mathcal{D}}\omega^2\tilde{\zeta}+\partial_Z\tilde{\sigma}_{zz} &= 0, && (41)
\end{aligned}
$$

where the hereby introduced visco-elastic extra terms $\tilde{\mathcal{I}}_P^F$, $\tilde{\mathcal{I}}_\sigma^F$, $\tilde{\mathcal{I}}_P^S$ and $\tilde{\mathcal{I}}_\sigma^S$ read

$$
\begin{aligned}
\tilde{\mathcal{I}}_P^F &= \left(\frac{\mathcal{C}_s^e}{\tilde{\mathcal{C}}_s}\right)^2\frac{1-\nu_e^2\tilde{\nu}_s+\frac{\alpha(2+\alpha)}{2}(1+\nu_e\tilde{\nu}_s)}{1-\nu_e^2+\frac{\alpha(2+\alpha)}{2}(1+\nu_e)}-1\equiv\frac{1}{\tilde{E}_s(\omega)}\frac{1-\nu_e^2\tilde{\nu}_s(\omega)+\frac{\alpha(2+\alpha)}{2}(1+\nu_e\tilde{\nu}_s(\omega))}{1-\nu_e^2+\frac{\alpha(2+\alpha)}{2}(1+\nu_e)}-1, && (42)\\
\tilde{\mathcal{I}}_\sigma^F &= \left(\frac{\mathcal{C}_s^e}{\tilde{\mathcal{C}}_s}\right)^2(\tilde{\nu}_s(\omega)-1)\equiv\frac{\tilde{\nu}_s(\omega)-1}{\tilde{E}_s(\omega)}, && (43)\\
\tilde{\mathcal{I}}_P^S &= \tilde{\nu}_s-1+\tilde{\nu}_s\frac{\mathcal{C}_s^{e2}-\tilde{\mathcal{C}}_s^2}{\tilde{\mathcal{C}}_s^2}\equiv-\left(1-\frac{\tilde{\nu}_s(\omega)}{\tilde{E}(\omega)}\right), && (44)\\
\tilde{\mathcal{I}}_\sigma^S &= \frac{\mathcal{C}_s^{e2}-\tilde{\mathcal{C}}_s^2}{\tilde{\mathcal{C}}_s^2}\equiv\frac{1-\tilde{E}_s(\omega)}{\tilde{E}_s(\omega)}. && (45)
\end{aligned}
$$

In (42)-(45), the relation $\tilde{\mathcal{C}}_s^2=\mathcal{C}_s^{e2}\tilde{E}_s$ have been used according to (14). The dimensionless visco-elastic Young modulus ratio in (42)-(45) are directly connected to the dimensionless, frequency-dependent, creep function $\tilde{J}_s(\omega)$, defined as

$$
\tilde{J}_s(\omega)-1=\frac{1-\tilde{E}_s}{\tilde{E}_s},\quad\text{or}\quad\tilde{J}_s(\omega)=\frac{1}{\tilde{E}_s}, \tag{46}
$$

so that, each visco-elastic kernel in (42)-(45) is linearly related to the creep function $\tilde{J}_s(\omega)$ which encapsulates part of their material rheology dependence. Nevertheless, (42)-(45) display supplementary frequency dependence of these kernels related to the visco-elastic Poisson coefficient $\tilde{\nu}_s(\omega)$ and the dimensionless Young modulus $\tilde{E}_s(\omega)$ defined in (11). Finally, it is interesting to state that the time-domain version of (39)-(41), i.e the inverse Fourier transform of (39)-(41) is the FSI four-equations formulation used for the method of characteristics since all l.h.s terms display constant convective hyperbolic operators associated with a constant travelling velocity. This choice has been set in order to provide the easiest comparison with previous formulations, such as [28]. However, the next section details another popular approach for visco-elastic propagation, i.e. the evaluation of a dispersive frequency-dependent visco-elastic velocity with its associated, wave propagation operator in the Fourier domain.

3.5. Pressure-stress coupled visco-elastic wave propagation

Let us now consider the three equations (38)-(39)-(40)-, which, from the elimination of $\tilde{\zeta}$ and $\tilde{W}$ produces the following forced wave equation for the pressure perturbation

$$
\omega^2\left[1+\chi_e\tilde{\mathcal{I}}_P^F+\frac{4\nu_e^2\mathcal{D}}{\alpha(2+\alpha)\mathcal{C}_s^{e2}}\left(1+\tilde{\mathcal{I}}_P^S\right)\right]\tilde{P}+\partial_Z^2\tilde{P}=\frac{2\nu_e\mathcal{D}}{\mathcal{C}_s^{e2}}\left(1+\tilde{\mathcal{I}}_\sigma^S+\tilde{\mathcal{I}}_P^F\right)\tilde{\sigma}_{zz}. \tag{47}
$$

This wave equation can then be rewritten using (40) and (41) on the right-hand-side of (47), whilst also using (43) and (45) to simplify the kernel's dependance

$$\omega^2 \tilde{P} + [\tilde{c}_p^v]^2 \partial_Z^2 \tilde{P} = 2\alpha \nu_e \tilde{\nu}_s \omega^2 [\tilde{c}_p^v]^2 \partial_Z \tilde{\zeta} \tag{48}$$

where the effective frequency-dependent corrective visco-elastic pulsed-wave speed $\tilde{c}_p^v(\omega)$ has been introduced

$$\tilde{c}_p^v(\omega) = \frac{1}{\sqrt{1 + \chi_e \tilde{\mathcal{I}}_P^F - \frac{4\mathcal{D}\nu_e^2}{\alpha(2+\alpha)\mathcal{C}_s^{e2}} \tilde{\mathcal{I}}_\sigma^F \frac{1+\tilde{\mathcal{I}}_P^S}{1+\tilde{\mathcal{I}}_\sigma^S}}}. \tag{49}$$

On the other hand, the coupled equations (40) and (41) give rise to the coupled stress/pressure wave equation in the solid

$$\left[1 + \tilde{\mathcal{I}}_\sigma^S\right] \omega^2 \tilde{\sigma}_{zz} + \mathcal{C}_s^{e2} \partial_Z^2 \tilde{\sigma}_{zz} = \frac{2\nu_e \omega^2}{\alpha(2+\alpha)} \left[1 + \tilde{\mathcal{I}}_P^S\right] \tilde{P}. \tag{50}$$

The wave system resulting from the FSI four equations hyperbolic problem (39)-(41) can thus be recast into two coupled waves propagating system associated with a two-component pressure/stress vector $\tilde{\mathbf{P}} \equiv [\tilde{P}, \tilde{\sigma}_{zz}]$ following [35]

$$\omega^2 \tilde{\mathbf{P}} + [\tilde{c}_p^v]^2 \begin{pmatrix} 1 & 2\nu_e \mathcal{D} \frac{1+\tilde{\mathcal{I}}_\sigma^S + \tilde{\mathcal{I}}_\sigma^F}{1+\tilde{\mathcal{I}}_\sigma^S} \\ \frac{2\nu_e}{\alpha(2+\alpha)} \frac{1+\tilde{\mathcal{I}}_P^S}{1+\tilde{\mathcal{I}}_\sigma^S} & \mathcal{C}_s^{e2} \frac{1+\chi_e \tilde{\mathcal{I}}_P^F}{1+\tilde{\mathcal{I}}_\sigma^S} + \frac{4\nu_e^2 \mathcal{D}}{\alpha(2+\alpha)} \frac{1+\tilde{\mathcal{I}}_P^S}{1+\tilde{\mathcal{I}}_\sigma^S} \end{pmatrix} \partial_Z^2 \tilde{\mathbf{P}} = \mathbf{0}. \tag{51}$$

The characteristic equation associated with this propagating operator is

$$\left(\frac{\tilde{c}_\pm}{\tilde{c}_p^v}\right)^4 - \left(\frac{\tilde{c}_\pm}{\tilde{c}_p^v}\right)^2 \left[1 + \mathcal{C}_s^{e2} \frac{1 + \chi_e \tilde{\mathcal{I}}_P^F}{1 + \tilde{\mathcal{I}}_\sigma^S} + \frac{4\nu_e^2 \mathcal{D}}{\alpha(2+\alpha)} \frac{1 + \tilde{\mathcal{I}}_P^S}{1 + \tilde{\mathcal{I}}_\sigma^S}\right] + \mathcal{C}_s^{e2} \frac{1 + \chi_e \tilde{\mathcal{I}}_P^F}{1 + \tilde{\mathcal{I}}_\sigma^S} + \frac{4\nu_e^2 \mathcal{D}}{\alpha(2+\alpha)} \frac{1 + \tilde{\mathcal{I}}_P^S}{1 + \tilde{\mathcal{I}}_\sigma^S} \left(1 - \frac{1 + \tilde{\mathcal{I}}_\sigma^S + \tilde{\mathcal{I}}_\sigma^F}{1 + \tilde{\mathcal{I}}_\sigma^S}\right) = 0, \tag{52}$$

the root of which can then be explicitly found

$$\tilde{c}_\pm^2 = [\tilde{c}_p^v]^2 \frac{\hat{c} \pm \sqrt{\hat{c}^2 - 4\left[\mathcal{C}_s^{e2} \frac{1+\chi_e \tilde{\mathcal{I}}_P^F}{1+\tilde{\mathcal{I}}_\sigma^S} + \frac{4\nu_e^2 \mathcal{D}}{\alpha(2+\alpha)} \frac{1+\tilde{\mathcal{I}}_P^S}{1+\tilde{\mathcal{I}}_\sigma^S} \left(1 - \frac{1+\tilde{\mathcal{I}}_\sigma^S + \tilde{\mathcal{I}}_\sigma^F}{1+\tilde{\mathcal{I}}_\sigma^S}\right)\right]}}{2}, \tag{53}$$

$$\hat{c} = 1 + \mathcal{C}_s^{e2} \frac{1 + \chi_e \tilde{\mathcal{I}}_P^F}{1 + \tilde{\mathcal{I}}_\sigma^S} + \frac{4\nu_e^2 \mathcal{D}}{\alpha(2+\alpha)} \frac{1 + \tilde{\mathcal{I}}_P^S}{1 + \tilde{\mathcal{I}}_\sigma^S} \equiv \frac{\tilde{c}_+^2 + \tilde{c}_-^2}{[\tilde{c}_p^v]^2}. \tag{54}$$

The diagonalisation matrix of (51) operator along with the change of basis relations are

$$\tilde{\mathbf{\Pi}}(\omega) = \begin{pmatrix} \frac{2\nu_e \mathcal{D}[\tilde{c}_p^v]^2}{\tilde{c}_-^2 - [\tilde{c}_p^v]^2} \frac{1+\tilde{\mathcal{I}}_\sigma^S + \tilde{\mathcal{I}}_\sigma^F}{1+\tilde{\mathcal{I}}_\sigma^S} & \frac{2\nu_e \mathcal{D}[\tilde{c}_p^v]^2}{\tilde{c}_+^2 - [\tilde{c}_p^v]^2} \frac{1+\tilde{\mathcal{I}}_\sigma^S + \tilde{\mathcal{I}}_\sigma^F}{1+\tilde{\mathcal{I}}_\sigma^S} \\ 1 & 1 \end{pmatrix} \quad \text{, and} \quad \tilde{\boldsymbol{\mathcal{P}}} = \tilde{\mathbf{\Pi}}^{-1} \tilde{\mathbf{P}} = \begin{pmatrix} \tilde{\mathcal{P}}^- \\ \tilde{\mathcal{P}}^+ \end{pmatrix}. \tag{55}$$

The wave-vector system (51) then becomes diagonal

$$\left[\omega^2 + \begin{pmatrix} \tilde{c}_-^2 & 0 \\ 0 & \tilde{c}_+^2 \end{pmatrix} \partial_Z^2\right] \tilde{\boldsymbol{\mathcal{P}}} = \mathbf{0}. \tag{56}$$

From (56) it is then possible to find the explicit (Z,ω) dependence of $\tilde{\boldsymbol{\mathcal{P}}}(Z,\omega)$ (as well as its gradient) which depends upon the prescribed boundary condition $\left(\tilde{\mathcal{P}}^{\pm}(0,\omega), \partial_Z\tilde{\mathcal{P}}^{\pm}(0,\omega)\right)$ as

$$\tilde{\mathcal{P}}^{\pm}(Z,\omega) = \cos\left(\frac{\omega}{\tilde{c}_{\pm}}Z\right)\tilde{\mathcal{P}}^{\pm}(0,\omega) + \sin\left(\frac{\omega}{\tilde{c}_{\pm}}Z\right)\left[\frac{\tilde{c}_{\pm}}{\omega}\partial_Z\tilde{\mathcal{P}}^{\pm}(0,\omega)\right], \tag{57}$$

$$\partial_Z\tilde{\mathcal{P}}^{\pm}(Z,\omega) = -\frac{\omega}{\tilde{c}_{\pm}}\sin\left(\frac{\omega}{\tilde{c}_{\pm}}Z\right)\tilde{\mathcal{P}}^{\pm}(0,\omega) + \cos\left(\frac{\omega}{\tilde{c}_{\pm}}Z\right)\partial_Z\tilde{\mathcal{P}}^{\pm}(0,\omega). \tag{58}$$

4. Analysis of an experimental configuration using explicit visco-elastic rheology

The herein rheology-based model is now explicitly derived for a single pipe closed valve configuration, also known as the reservoir-pipe-anchored valve problem. Hereafter, general visco-elastic rheology is considered which allows the analytical derivation of the pressure-stress vector solution $\tilde{\mathbf{P}}$, along with explicit expressions for visco-elastic convolution kernels (42)-(45).

4.1. Generalized 3D visco-elastic rheology

Various Kelvin-Voigt models have been previously considered in the literature [43, 32, 21, 22, 23, 29]. Nevertheless, for a real solid a 3D rheological model is necessary to take care of the solid's shape (not necessarily 1D/isotropic/spherical) and the considered boundary conditions. A general form of 3D visco-elastic rheology reads

$$a\left(1+\tau_r\partial_t\right)\boldsymbol{\sigma}_s^* = \lambda_e\left(1+\tau_\lambda\partial_t\right)\left(\boldsymbol{\nabla}\cdot\boldsymbol{\xi}^*\right)\mathbf{I} + \mu_e\left(1+\tau_\mu\partial_t\right)\left(\boldsymbol{\nabla}\boldsymbol{\xi}^* + \boldsymbol{\nabla}^T\boldsymbol{\xi}^*\right), \tag{59}$$

where six parameters $a, \tau_r, \tau_\lambda, \tau_\mu, \lambda_e, \mu_e$ can be used as constitutive ones, whilst (λ_e, μ_e) being the elastic Lamé coefficients and $(\tau_r, \tau_\lambda, \tau_\mu)$ are characteristic times, all independent from ω^*. Various 3D visco-elastic rheological laws have indeed been considered in the literature [3, 15, 44, 45, 46, 47, 48], (59) encapsulating all of those. More precisely, all model parameters of the cited references, are provided in table 1. It is important to note that most of the visco-elastic models proposed in literature did not consider the relaxation parameter τ_r associated with the instantaneous elastic response. Only [15] consider this term for an incompressible material. Now, from the Fourier

	a	τ_r	λ_e	τ_λ	μ_e	τ_μ
Carcione et al. [44]			✓	✓	✓	✓
Eringen, Canic et al.[45, 3]			✓	✓	✓	✓
Kisilova et al. [15]		✓			✓	✓
Bland [46]			✓		✓	
Ieşan [47]			✓	✓	✓	✓
Sharma et al. [48]			✓	✓	✓	✓

Table 1: Comparative table of 3D rheological parameters taken from literature.

transform of (59) and identification with (7) the generalized Lamé coefficients can be deduced for

this rheology

$$\tilde{\lambda}_s^*(\omega^*) = \lambda_e \frac{1+i\omega^*\tau_\lambda}{a\,(1+i\omega^*\tau_r)} \quad \text{, and} \quad \tilde{\mu}_s^*(\omega^*) = \mu_e \frac{1+i\omega^*\tau_\mu}{a\,(1+i\omega^*\tau_r)}. \tag{60}$$

Generalized Poisson and Young modulus can also be found from these rheological parameters

$$\tilde{\nu}_s^*(\omega^*) = \nu_e \frac{1+i\omega^*\tau_\lambda}{1+i\omega^*\tau_\nu} \quad \text{, and} \quad \tilde{E}_s^*(\omega^*) = \frac{E_e(1+i\omega^*\tau_\mu)(1+i\omega^*\tau_E)}{a(1+i\omega^*\tau_r)(1+i\omega^*\tau_\nu)}, \tag{61}$$

where the above introduced times-scale τ_ν and τ_E are given by

$$\tau_\nu = \frac{\lambda_e\tau_\lambda + \mu_e\tau_\mu}{\lambda_e+\mu_e} \quad \text{, and} \quad \tau_E = \frac{3\lambda_e\tau_\lambda + 2\mu_e\tau_\mu}{3\lambda_e+2\mu_e}. \tag{62}$$

Also, the dimensionless creep function $\tilde{J}_s(\omega)$ (46) reads regarding (6) and (9)

$$\tilde{J}_s(\omega) = \frac{1}{\tilde{E}_s} = a\frac{\left(1+i\omega\tau_r\frac{c_p^e}{L}\right)\left(1+i\omega\tau_\nu\frac{c_p^e}{L}\right)}{\left(1+i\omega\tau_\mu\frac{c_p^e}{L}\right)\left(1+i\omega\tau_E\frac{c_p^e}{L}\right)}. \tag{63}$$

4.1.1. Explicit form of visco-elastic extra-terms kernels

As discussed in S.2.2, the motivation of this study is to built a rheology-based model dependent on the material visco-elastic properties but not on the specific wave problem and/or its boundary conditions. For this the visco-elastic kernels are now explicitly derived versus rheological parameters. In the 3D visco-elastic rheology model framework, the rheological parameters $\left(\tilde{\nu}_s^*, \tilde{E}_s^*\right)$ presented in (11) and (61), are explicit function of the characteristic times $(\tau_\lambda, \tau_\mu, \tau_\nu, \tau_E, \tau_r)$ presented in (62) as well as elastic parameters. The convolution visco-elastic kernels (42)-(45) can thus be explicitly found

$$\tilde{\mathcal{I}}_P^F = a\frac{\left(1+i\omega\tau_r\frac{c_p^e}{L}\right)\left(1+i\omega\tau_\nu\frac{c_p^e}{L}\right)}{\left(1+i\omega\tau_\mu\frac{c_p^e}{L}\right)\left(1+i\omega\tau_E\frac{c_p^e}{L}\right)} \frac{\nu_e^2\frac{1+i\omega\tau_\lambda\frac{c_p^e}{L}}{1+i\omega\tau_\nu\frac{c_p^e}{L}} - 1 - \frac{\alpha(2+\alpha)}{2}\left(1+\nu_e\frac{1+i\omega\tau_\lambda\frac{c_p^e}{L}}{1+i\omega\tau_\nu\frac{c_p^e}{L}}\right)}{\nu_e^2 - 1 - \frac{\alpha(2+\alpha)}{2}(1+\nu_e)} - 1, \tag{64}$$

$$\tilde{\mathcal{I}}_\sigma^F = a\frac{\left(1+i\omega\tau_r\frac{c_p^e}{L}\right)\left(1+i\omega\tau_\nu\frac{c_p^e}{L}\right)}{\left(1+i\omega\tau_\mu\frac{c_p^e}{L}\right)\left(1+i\omega\tau_E\frac{c_p^e}{L}\right)} \left(\frac{1+i\omega\tau_\lambda\frac{c_p^e}{L}}{1+i\omega\tau_\nu\frac{c_p^e}{L}} - 1\right), \tag{65}$$

$$\tilde{\mathcal{I}}_P^S = -\left(1 - a\frac{\left(1+i\omega\tau_r\frac{c_p^e}{L}\right)\left(1+\omega\tau_\lambda\frac{c_p^e}{L}\right)}{\left(1+i\omega\tau_\mu\frac{c_p^e}{L}\right)\left(1+i\omega\tau_E\frac{c_p^e}{L}\right)}\right), \tag{66}$$

$$\tilde{\mathcal{I}}_\sigma^S = -\left(1 - a\frac{\left(1+i\omega\tau_r\frac{c_p^e}{L}\right)\left(1+i\omega\tau_\nu\frac{c_p^e}{L}\right)}{\left(1+i\omega\tau_\mu\frac{c_p^e}{L}\right)\left(1+i\omega\tau_E\frac{c_p^e}{L}\right)}\right). \tag{67}$$

Using the inverse Fourier transform, their time-domain form read

$$\mathcal{I}_P^F = \frac{\frac{a}{\mathcal{C}_\nu}\tau_r\left[\nu_e\tau_\lambda\left(\nu_e-\frac{\alpha(2+\alpha)}{2}\right)-\tau_\nu\left(\frac{\alpha(2+\alpha)}{2}+1\right)\right]-\tau_E\tau_\mu}{\tau_E\tau_\mu}\delta(\tau)$$
$$+\frac{aL(\tau_E-\tau_r)\left(\nu_e(\tau_\lambda-\tau_E)\left(\frac{\alpha(2+\alpha)}{2}-\nu_e\right)+(\tau_\nu-\tau_E)\left(\frac{\alpha(2+\alpha)}{2}+1\right)\right)}{c_p^e\tau_E^2\mathcal{C}_\nu(\tau_E-\tau_\mu)}e^{-\frac{\tau L}{\tau_E c_p^e}}H(\tau)$$
$$+\frac{aL(\tau_\mu-\tau_r)\left(\nu_e(\tau_\mu-\tau_\lambda)\left(\frac{\alpha(2+\alpha)}{2}-\nu_e\right)+(\tau_\mu-\tau_\nu)\left(\frac{\alpha(2+\alpha)}{2}+1\right)\right)}{c_p^e\tau_\mu^2\mathcal{C}_\nu(\tau_E-\tau_\mu)}e^{-\frac{\tau L}{\tau_\mu c_p^e}}H(\tau), \quad (68)$$

$$\mathcal{I}_\sigma^F = \frac{a\tau_r(\tau_\lambda-\tau_\nu)}{\tau_E\tau_\mu}\delta(\tau)-\frac{aL(\tau_\lambda-\tau_\nu)}{c_p^e\tau_E^2\tau_\mu^2(\tau_E-\tau_\mu)}\left(\tau_\mu^2(\tau_E-\tau_r)e^{-\frac{\tau L}{\tau_E c_p^e}}-\tau_E^2(\tau_\mu-\tau_r)e^{-\frac{\tau L}{\tau_\mu c_p^e}}\right)H(\tau), \quad (69)$$

$$\mathcal{I}_P^S = \frac{a\tau_\lambda\tau_r-\tau_E\tau_\mu}{\tau_E\tau_\mu}\delta(\tau)+\frac{aL}{c_p^e(\tau_E-\tau_\mu)}\left(\frac{(\tau_E-\tau_r)(\tau_E-\tau_\lambda)}{\tau_E}\frac{e^{-\frac{\tau L}{\tau_E c_p^e}}}{\tau_E}-\frac{(\tau_\mu-\tau_r)(\tau_\mu-\tau_\lambda)}{\tau_\mu}\frac{e^{-\frac{\tau L}{\tau_\mu c_p^e}}}{\tau_\mu}\right)H(\tau), \quad (70)$$

$$\mathcal{I}_\sigma^S = \frac{a\tau_\nu\tau_r-\tau_E\tau_\mu}{\tau_E\tau_\mu}\delta(\tau)+\frac{aL}{c_p^e(\tau_E-\tau_\mu)}\left(\frac{(\tau_E-\tau_r)(\tau_E-\tau_\nu)}{\tau_E}\frac{e^{-\frac{\tau L}{\tau_E c_p^e}}}{\tau_E}-\frac{(\tau_\mu-\tau_r)(\tau_\mu-\tau_\nu)}{\tau_\mu}\frac{e^{-\frac{\tau L}{\tau_\mu c_p^e}}}{\tau_\mu}\right)H(\tau), \quad (71)$$

where $\delta(\tau)$ and $H(\tau)$ stands for the Dirac distribution and its primitive, the Heaviside function. Relations (68)-(71) have been cross-checked using formal calculus software. It is interesting to note that every r.h.s of(68)-(71) display a Dirac distribution term resulting in a *local* visco-elastic response thus modifying the elastic one. In other words, these terms being independent of ω in Fourier space (the Fourier transform of the Dirac distribution is equal to one) they act as a modification of the non-dispersive elastic wave-speed. We will more explicitly examine how this provides an additional visco-elastic contribution to the elastic velocity in the next section. However it is interesting to mention that the choice for defining kernels $\tilde{\mathcal{I}}_P^F, \tilde{\mathcal{I}}_\sigma^F, \tilde{\mathcal{I}}_P^S, \tilde{\mathcal{I}}_\sigma^S$ has been done in order to permit a better comparison with previous models. However, local terms could have been recast into some elastic-like behaviour resulting from visco-elastic effects and left aside the kernels.

4.2. The reservoir-pipe-anchored valve problem

As depicted in Figure 1, the single visco-elastic pipe anchored upstream to a reservoir and downstream to an instantaneous closure valve, is now investigated. In the following the experimental data of Covas et al. ([19, 13]) and Pezinga et al. [33] are investigated, the details of which are given in Table 2. The perturbed flow rate is set to $Q_0 = 1.01\ l/s$ and $Q_0 = 4.03\ l/s$ for the experiments of Covas et al., [19, 13] and Pezinga et al., [33], respectively. For the investigated

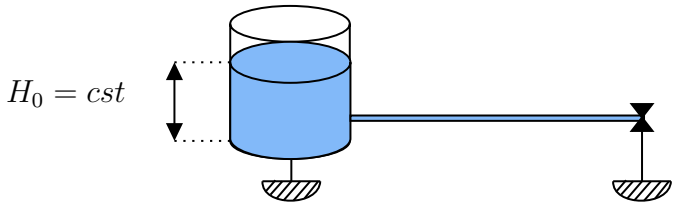

Figure 1: Constant head H_0 reservoir-pipe-anchored valve configuration

systems, the elastic fluid pulse wave speed is found equal to $c_p^e = 394.6m/s$ and $c_p^e = 360.05m/s$ respectively for Covas et al. ([19, 13]) and Pezzinga et al. [33] experimental set up. Upstream, the reservoir impedes the pressure to fluctuate whereas downstream, a sudden velocity perturbation is imposed, the result of which is a pressure gradient variation according to (39). Downstream, the velocity variation associated with an impulse response is thus $W(1,t) = -H(t)$(here again

Ref	$(\mathrm{kg}\cdot\mathrm{m}^{-3})$	Elas. (Pa)	ν_f $(\mathrm{m}^2\cdot\mathrm{s}^{-1})$	ν_e	c_p^e $(\mathrm{m}\cdot\mathrm{s}^{-1})$	δ	Geom.(m)
[19, 13]	$\rho_f = 998.3$	$\mathcal{K}_f = 2.1\cdot 10^9$	10^{-6}	0.46	394.56	$4.6\ 10^{-2}$	$R_0 = 2.53\cdot 10^{-2}$
	$\rho_s = 960.0$	$E_e = 1.43\cdot 10^9$					$e = 6.3\cdot 10^{-3}$
							$L = 277.0$
[33]	$\rho_f = 998.3$	$\mathcal{K}_f = 2.1\cdot 10^9$	10^{-6}	0.45	359.25	$1.6\ 10^{-2}$	$R_0 = 4.67\cdot 10^{-2}$
	$\rho_s = 960.0$	$E_e = 1.56\cdot 10^9$					$e = 8.1\cdot 10^{-3}$
							$L = 200.0$

Table 2: Physical and geometrical properties for the experimental visco-elastic analysis of the reservoir-pipe-anchored valve system of Covas et al. ([19, 13]) and Pezinga et al. [33] using HDPE material and water. The c_p^e reported are evaluated using parameters provided in the table using relation (1). A slightly different values $c_p^e = 339\mathrm{m}\cdot\mathrm{s}^{-1}$ is reported in [33] using a different expression than (1) for c_p^e. In Covas et al. [19, 13] a range of E_e values provides a range of value $380 - 435\mathrm{m}\cdot\mathrm{s}^{-1}$ for c_p^e consistent with the hereby deduced value. Water hammer dimensionless number δ has been evaluated with (87).

$H(t)$ is the Heaviside function), being minus one for positive time. This transient closure law is set to compensate steady-state velocity (being one at time zero) with initial transient conditions $W(Z, t = 0) = 0$. The Fourier transform of $W(1, t)$ for $\omega > 0$ is thus precisely $\tilde{W}(1, \omega) = -i/\omega$ leading to $\partial_Z \tilde{P}(1, \omega) = 1 \equiv i\omega\tilde{W}(1, w)$ from (34). The pipe is supposed anchored at both ends so that no solid motion occurs, i.e. $\tilde{\zeta}(Z = 0, \omega) = \tilde{\zeta}(Z = 1, \omega) = 0$, which is equivalent to cancel-out the solid stress gradient according to (41). In the original basis, the boundary conditions read

$$\tilde{P}(0, \omega) = 0 \quad , \partial_Z \tilde{P}(1, \omega) = 1, \quad \partial_Z \tilde{\sigma}_{zz}(0, \omega) = \partial_Z \tilde{\sigma}_{zz}(1, \omega) = 0. \tag{72}$$

Introducing

$$\tilde{\beta}(\omega) = \frac{\tilde{c}_+}{\tilde{c}_-} \cdot \frac{\tilde{c}_-^2 - \left(\tilde{c}_p^v\right)^2}{\tilde{c}_+^2 - \left(\tilde{c}_p^v\right)^2}, \tag{73}$$

the diagonal-space vector boundary conditions can be deduced from (55), (58) and (72)

$$\tilde{\mathcal{P}}^-(0, \omega) = -\frac{\tilde{c}_-\tilde{\beta}}{\tilde{c}_+}\tilde{\mathcal{P}}^+(0, \omega), \tag{74}$$

$$\partial_Z\tilde{\mathcal{P}}^-(0, \omega) = -\partial_Z\tilde{\mathcal{P}}^+(0, \omega), \tag{75}$$

$$\partial_Z\tilde{\mathcal{P}}^-(1, \omega) = -\frac{\omega}{\tilde{c}_-}\sin\left(\frac{\omega}{\tilde{c}_-}\right)\tilde{\mathcal{P}}^-(0, \omega) + \cos\left(\frac{\omega}{\tilde{c}_-}\right)\partial_Z\tilde{\mathcal{P}}^-(0, \omega) = \frac{\tilde{c}_-^2 - \left(\tilde{c}_p^v\right)^2}{2\nu_e\mathcal{D}\left(\tilde{c}_p^v\right)^2\left(1 - \frac{\tilde{c}_-\tilde{\beta}}{\tilde{c}_+}\right)}\frac{1 + \tilde{\mathcal{I}}_\sigma^S}{1 + \tilde{\mathcal{I}}_\sigma^S + \tilde{\mathcal{I}}_\sigma^F}, \tag{76}$$

$$\partial_Z\tilde{\mathcal{P}}^+(1, \omega) = \frac{\omega}{\tilde{c}_-\tilde{\beta}}\sin\left(\frac{\omega}{\tilde{c}_+}\right)\tilde{\mathcal{P}}^-(0, \omega) - \cos\left(\frac{\omega}{\tilde{c}_+}\right)\partial_Z\tilde{\mathcal{P}}^-(0, \omega) = -\frac{\tilde{c}_-^2 - \left(\tilde{c}_p^v\right)^2}{2\nu_e\mathcal{D}\left(\tilde{c}_p^v\right)^2\left(1 - \frac{\tilde{c}_-\tilde{\beta}}{\tilde{c}_+}\right)}\frac{1 + \tilde{\mathcal{I}}_\sigma^S}{1 + \tilde{\mathcal{I}}_\sigma^S + \tilde{\mathcal{I}}_\sigma^F}. \tag{77}$$

Defining matrix $\tilde{\mathbf{M}}(\omega)$ as

$$\tilde{\mathbf{M}}(\omega) \equiv \begin{pmatrix} -\frac{\omega}{\tilde{c}_-}\sin\left(\frac{\omega}{\tilde{c}_-}\right) & \cos\left(\frac{\omega}{\tilde{c}_-}\right) \\ \frac{\omega\sin\left(\frac{\omega}{\tilde{c}_+}\right)}{\tilde{c}_-\tilde{\beta}} & -\cos\left(\frac{\omega}{\tilde{c}_+}\right) \end{pmatrix}. \tag{78}$$

The boundary condition system (74)-(77) can be expressed in the following matrix form

$$\tilde{\mathbf{M}}(\omega)\cdot\begin{pmatrix}\tilde{\mathcal{P}}^-\\ \partial_Z\tilde{\mathcal{P}}^-\end{pmatrix}(0,\omega)=\frac{\tilde{c}_-^2-\left(\tilde{c}_p^v\right)^2}{2\nu_e\mathcal{D}\left(\tilde{c}_p^v\right)^2\left(1-\frac{\tilde{c}_-\tilde{\beta}}{\tilde{c}_+}\right)}\frac{1+\tilde{\mathcal{I}}_\sigma^S}{1+\tilde{\mathcal{I}}_\sigma^S+\tilde{\mathcal{I}}_\sigma^F}\begin{pmatrix}1\\ -1\end{pmatrix}. \tag{79}$$

Multiplying (79) by $\tilde{\mathbf{M}}^{-1}(\omega)$ leads to

$$\begin{pmatrix}\tilde{\mathcal{P}}^-\\ \partial_Z\tilde{\mathcal{P}}^-\end{pmatrix}(0,\omega) = -\frac{\tilde{c}_-^2-\left(\tilde{c}_p^v\right)^2}{2\nu_e|\tilde{\mathbf{M}}|\mathcal{D}\left(\tilde{c}_p^v\right)^2\left(1-\frac{\tilde{c}_-\tilde{\beta}}{\tilde{c}_+}\right)}\frac{1+\tilde{\mathcal{I}}_\sigma^S}{1+\tilde{\mathcal{I}}_\sigma^S+\tilde{\mathcal{I}}_\sigma^F}\begin{pmatrix}\cos\left(\frac{\omega}{\tilde{c}_+}\right)-\cos\left(\frac{\omega}{\tilde{c}_-}\right)\\ \frac{\omega}{\tilde{c}_-}\left[\frac{\sin\left(\frac{\omega}{\tilde{c}_+}\right)}{\tilde{\beta}}-\sin\left(\frac{\omega}{\tilde{c}_-}\right)\right]\end{pmatrix}, \tag{80}$$

with $|\tilde{\mathbf{M}}|(\omega)\equiv\det\left(\tilde{\mathbf{M}}\right)$ given by

$$|\tilde{\mathbf{M}}|(\omega)=\frac{\omega}{\tilde{c}_-}\left[\sin\left(\frac{\omega}{\tilde{c}_-}\right)\cos\left(\frac{\omega}{\tilde{c}_+}\right)-\frac{1}{\tilde{\beta}}\sin\left(\frac{\omega}{\tilde{c}_+}\right)\cos\left(\frac{\omega}{\tilde{c}_-}\right)\right]. \tag{81}$$

Combining (80), (81) and (74) in (57) close the diagonal wave solution in Fourier domain reading

$$\tilde{\boldsymbol{\mathcal{P}}}(Z,\omega)=\tilde{\mathcal{P}}^-(0,\omega)\begin{pmatrix}\cos\left(\frac{\omega Z}{\tilde{c}_-}\right)\\ -\frac{\tilde{c}_+}{\tilde{c}_-\tilde{\beta}}\cos\left(\frac{\omega Z}{\tilde{c}_+}\right)\end{pmatrix}+\frac{\partial_Z\tilde{\mathcal{P}}^-(0,\omega)}{\omega}\begin{pmatrix}\tilde{c}_-\sin\left(\frac{\omega Z}{\tilde{c}_-}\right)\\ -\tilde{c}_+\sin\left(\frac{\omega Z}{\tilde{c}_+}\right).\end{pmatrix} \tag{82}$$

Or, in a more explicit and compact form

$$\tilde{\boldsymbol{\mathcal{P}}}(Z,\omega)=-\frac{\tilde{c}_-^2-\left(\tilde{c}_p^v\right)^2}{2\nu_e|\tilde{\mathbf{M}}|\mathcal{D}\left(\tilde{c}_p^v\right)^2\left(1-\frac{\tilde{c}_-\tilde{\beta}}{\tilde{c}_+}\right)}\frac{1+\tilde{\mathcal{I}}_\sigma^S}{1+\tilde{\mathcal{I}}_\sigma^S+\tilde{\mathcal{I}}_\sigma^F}\begin{pmatrix}\left[\cos\left(\frac{\omega}{\tilde{c}_+}\right)-\cos\left(\frac{\omega}{\tilde{c}_-}\right)\right]\cos\left(\frac{\omega Z}{\tilde{c}_-}\right)+\frac{\sin\left(\frac{\omega}{\tilde{c}_+}\right)-\tilde{\beta}\sin\left(\frac{\omega}{\tilde{c}_-}\right)}{\tilde{\beta}}\sin\left(\frac{\omega Z}{\tilde{c}_-}\right)\\ -\frac{\tilde{c}_+}{\tilde{c}_-\tilde{\beta}}\left(\left[\cos\left(\frac{\omega}{\tilde{c}_+}\right)-\cos\left(\frac{\omega}{\tilde{c}_-}\right)\right]\cos\left(\frac{\omega Z}{\tilde{c}_+}\right)+\left[\sin\left(\frac{\omega}{\tilde{c}_+}\right)-\tilde{\beta}\sin\left(\frac{\omega}{\tilde{c}_-}\right)\right]\sin\left(\frac{\omega Z}{\tilde{c}_+}\right)\right)\end{pmatrix}. \tag{83}$$

4.3. Numerical Fast Fourier Transform (FFT) inversion procedure

The pressure-stress solution (83) has a simple pole in $\omega=0$ associated with the trivial zero of $|\tilde{\mathbf{M}}|$ (81), the contribution of which is equal to average signal in the time domain. The solution in the time domain is difficult to obtain first because of the discrete non-trivial set of poles from condition $|\tilde{\mathbf{M}}|=0$, and second from the square-root dependence of velocity $\tilde{c}_+$ (Cf (53)) leading to a branch-cut. Hence, the inverse Fourier transform of (83) is numerically computed with a homemade *Python* code and the use of the *Scipy.fft* library.

Experimental data analysis. The steady-pressure time-dependent experimental variations have been disregarded withdrawing the initial static head value to the pressure signal. The transient component has been scaled according to Joukowsky's theory [37, 38] (Cf. eq.(20)) and the physical time on the water-hammer advective one (Cf. eq.(4)). Then, the signal linear time-drift between the beginning and the end of the experimental pressure measurements is removed so as to analyse the effect of perturbations only, removing the change in the steady-state provided by the valve aperture. A Fast-Fourier-Transform (FFT) of the experimental time-dependent signal is performed providing their frequency-dependent counterpart. This FFT analysis is useful for the establishment of a suitable frequency threshold ensuring the Nyquist criterium, i.e. frequency truncation,

value to perform the inverse numerical FFT of (83). A cutoff frequency of $f_c = 2000Hz$ is found for both the experimental data sets.

Inverse Fast Fourier Transform (IFFT) of the theoretical pressure-stress solution. The dimensionless pulsation and time resolution are set equal to $\Delta\omega = 10^{-3}$ and $\Delta\tau = 2.5 \cdot 10^{-4}$, respectively, providing a frequency cutoff at $f_c = 2000Hz$. At this stage, the direct inverse Fourier transform of (83) cannot be performed from the ignorance of the rheological parameters $[a, \tau_r, \tau_\mu, \tau_\lambda]$. This is where the calibration procedure enters into play so as to minimise the quadratic error (using *"Scipy.optimize.curve_fit" Pyhton*'s library) between (83)'s IFFT and the experimental data in time domain, at the very same time-located points. If needed, a linear interpolation of (83)'s IFFT is used to perfectly match experimental time and numerical one. The calibration results are given below (for dimensionless parameters, as dicussed above) for the datasets of Covas et al. and Pezzinga et al.

$$[a, \tau_r, \tau_\mu, \tau_\lambda] \approx [1.3017, 0.1963, 0.3008, 0.1291] \quad \text{for Covas et al., [19, 13] data,} \tag{84}$$

$$[a, \tau_r, \tau_\mu, \tau_\lambda] \approx [1.1771, 0.1963, 0.2709, 0.1299] \quad \text{for Pezzinga et al., [33] data.} \tag{85}$$

It is interesting to observe that these calibrated dimensionless visco-elastic parameters are quite close although the two experiments were performed by two distinct teams in two distinct publications. However this can be understood from realising that the considered materials (HDPE) had closed mechanical properties, as provided in table 2. Also, the choice for using dimensionless parameters rather than dimensional ones permits to test their similarity independantly from the particular experimental set-up properties. The calibration procedure is thus comforted by this coherent estimation.

4.4. Comparison between fluid viscous dissipation, elastic FSI effects and visco-elastic effects

As mentioned in the introduction, viscous dissipation in the fluid boundary-layers is a supplementary source of damping, eventually less dissipative than visco-elastic effects as discussed in [14]. To illustrate this point, this section compares the fluid viscous dissipation with various visco-elastic models and the one observed in experiments. The fluid viscous dissipation brilliantly investigated by [16] without considering FSI effects is used for this purpose. Furthermore, to complement this comparison this section also analyses the influence of FSI effects in visco-elastic models. In the case of a reservoir-pipe-anchored valve system, Mei and Jing [16] derived an analytical exponential decay H_k, both mode and time dependent, for the pressure time domain variation

$$H_k = e^{-\sqrt{\frac{\lambda_k}{2}}\delta\tau} \quad \text{, with,} \quad \lambda_k = \quad \pi\left(\frac{1}{2} + k\right) \text{for,} \quad k \in \mathbf{N}, \tag{86}$$

so that Mei and Jing [16] rediscover the cornerstone role of the small dimensionless water-hammer dimensionless number

$$\delta = \sqrt{\frac{\nu_f L}{c_p^e R_0^2}}, \tag{87}$$

in the viscous boundary-layers exponential damping (this parameter was known of importance from many other previous studies). Recently, [35] provided a time-dependent solution for the elastic liquid-filled pipe FSI elastic response on the very same reservoir-pipe-anchored valve configuration but disregarded the effect of fluid viscosity. [35] derived a spectral transcendental equation governing the elastic resonant frequencies, the structure of which is found close to (81) when elastic

parameters are considered only. The visco-elastic pressure at the valve, i.e. $Z = 1$, for the experiment of Pezinga et al., [33] is depicted in Figure 2a along with its elastic counterpart where fluid viscous damping and FSI effects have been evaluated using the Method of Characteristics (MOC) [49] (figures 2a-2b) and Bayle and Plouraboué [35] (figures 2c-2d), respectively. For the viscous damping solved by the MOC method, Darcy-Weisbach model for unsteady friction and Zielke's kernel to take into account retarded fluid viscous effects have been used [49] with a time-step of $1.110^{-2}s$ into the single pipe configuration of Pezinga et al., [33]. One can observe in figures 2a that the fluid viscous damping is small compared to the visco-elastic one, as previously mentioned. Furthermore, the purely elastic FSI effect illustrated in figures 2c produces high-frequency response to the signal that are not visible in Pezinga et al., [33] experimental observations. Also, these high-frequencies are not clearly visible in the frequency domain either, as illustrated in figure 2d. Nevertheless both elastic non-FSI (figure 2b) and FSI predictions figure 2d accurately capture the first-two lowest frequency observed in Pezinga et al. [33]'s signal. Finally it is interesting to observe that visco-elastic FSI effects are interesting to consider in order to more accurately describe Pezinga et al. [33] pressure time variations as illustrated in figure 2e. Hence figure 2 illustrates the strong impact of the visco-elastic response to the pressure signal which displays a much stronger decay than the one found from viscous dissipation in the fluid [14]. This figure shows that the proposed visco-elastic theory permits a convincing description of the experimental pressure signature both in time and frequency domains. For longer times, the elastic and visco-elastic predictions rapidly diverge from each other. This is also consistent with the fact that for this long time, i.e smallest frequency, the corrective velocity $\tilde{c}_p^v$ is dissipative and strongly depends on frequency (as latter-on reported in figure 4a). As expected, the visco-elastic FSI response much more strongly attenuates high-frequency oscillations than the elastic one. More precisely, the signal's high frequencies arising from FSI-couplings quickly attenuate from the influence of visco-elastic kernel convolution and are barely discernible after the wave's first back and forth. The spectrum analysis provided in Figure 2b reveals how much the visco-elastic response smoothens high-frequencies so that only the first three harmonics appear relevant. A small shift of the visco-elastic resonant frequency compared to the elastic ones provided by the red dotted lines of figure 2b is also found as previously noted in [50]. However, in the early stage of the signal the proposed theoretical model fails to accurately reproduce the observed pressure variations by $\approx 18\%$, so that the Joukowsky [37, 38] over-pressure is not exactly recovered from visco-elastic FSI effects at this position $Z = 1$. Nevertheless, the overall damping trend and phase seem correctly represented. The comparison of the proposed visco-elastic rheology-based model with previous Kelvin-Voigt models is now discussed.

4.5. Comparison with previous theoretical models.

In Fourier-domain, the dimensionless form of models proposed by Covas et al. [13], on the left, and Keramat et al. [28], on the right, reads

$$i\omega\tilde{W} = -\partial_Z\tilde{P}, \qquad i\omega\tilde{W} = -\partial_Z\tilde{P}, \tag{88}$$

$$i\omega\tilde{P} + \partial_Z\tilde{W} = -\frac{2\mathcal{D}}{\alpha\mathcal{C}_s^{e2}}i\omega\tilde{\mathcal{I}}_{Cov}\tilde{P}, \qquad i\omega\tilde{P} + \partial_Z\tilde{W} - 2i\omega\alpha\nu_e\partial_Z\tilde{\zeta} = -\frac{2\mathcal{D}\left(1-\nu_e^2\right)}{\alpha\mathcal{C}_s^{e2}}i\omega\tilde{\mathcal{I}}_{Ker}\tilde{P}, \tag{89}$$

$$i\omega\tilde{\sigma}_{zz} - i\omega\frac{\nu_e}{\alpha}\tilde{P} - i\omega\frac{\alpha\mathcal{C}_s^{e2}}{\mathcal{D}}\partial_Z\tilde{\zeta} = -i\omega\tilde{\mathcal{I}}_{ker}\tilde{\sigma}_{zz} + \frac{\nu_e}{\alpha}i\omega\tilde{\mathcal{I}}_{Ker}\tilde{P}, \tag{90}$$

$$\frac{\alpha}{\mathcal{D}}\omega^2\tilde{\zeta} + \partial_Z\tilde{\sigma}_{zz} = 0, \tag{91}$$

where $\tilde{\mathcal{I}}_{Cov}$ –resp. $\tilde{\mathcal{I}}_{Ker}$– is the Fourier transform of kernels proposed in Covas et al. [13] (resp. Keramat et al. [28]). The Covas et al. [13]'s model stands as a limit when ν_e tends to zeros of the Keramat et al. [28]'s one as the Poisson coupling vanishes, resulting in decoupling fluid axial dynamic to the solid's one. The dimensionless derivation of the Keramat et al. [28]'s model is provided in Appendix C. Both authors consider N_{kv} Kelvin-Voigt elements to build their convolution kernel interpreted as a creeping law, each having its own exponential times-decay τ_k, amplitudes J_k, to model their convolution kernels, [30]

$$\left(\tilde{\mathcal{I}}_{Cov}, \tilde{\mathcal{I}}_{Ker}\right) = \sum_{k=1}^{N_{kv}} \frac{E_e J_k}{1 + i\omega \frac{c_p^e \tau_k}{L}}. \tag{92}$$

The values of (τ_k, J_k) for both models are provided in Table 3 for the experimental set-up of [13]. It is very interesting to note that Covas et al. [13]'s and Keramat et al. [28]'s models both display

k	τ_k(s)	$J_k(10^{-10}$Pa)
1	0.05	1.060
2	0.5	0.933
3	1.5	1.120

(a) Model [13]

k	$\tau_k(s)$	$J_k(10^{-10}Pa)$
1	0.05	1.057
2	0.5	1.054
3	1.5	0.9051
4	5	0.2617
5	10	0.7456

(b) Model [28]

Table 3: Covas et al.[13] and Keramat et al. [28]'s convolution kernels parameters for the experimental data of Covas et al. [19, 13].

a very similar form compared to (39)-(41). Qualitatively, the visco-elastic material response can indeed be recasted into similar convolution products with pressure and axial stress. In order to make this comparison more precise it is interesting to consider the very same hypothesis that the generalized Young modulus ν_s^* equals the elastic one ν_e, i.e. $\tilde{\nu}_s = 1$, and the dimensionless tube's thickness is small, i.e. $\alpha \ll 1$, in which case the visco-elastic kernels (42)-(45) in frequency-domain simplify to

$$\tilde{\mathcal{I}}_P^F = \tilde{\mathcal{I}}_P^S = \tilde{\mathcal{I}}_\sigma^S = \tilde{J}_s(\omega) - 1 \quad \text{, and } \quad \tilde{\mathcal{I}}_\sigma^F = 0. \tag{93}$$

This simplified framework indeed provides a simple condition for the equivalence of formulation according, to (46) and (92)

$$\tilde{J}_s(\omega) \equiv 1 + \sum_{k=1}^{N_{kv}} \frac{E_e J_k}{1 + i\omega \frac{c_p^e \tau_k}{L}}. \tag{94}$$

Hence, within $\tilde{\nu}_s = 1$ ($\tilde{\nu}_s^* = \nu_e$) and $\alpha \to 0$ hypothesis, it is nice to observe that the l.h.s of (38) display a convolution product with the pressure only, as so does (43) when $\mathcal{I}_\sigma^F = 0$ as provided by (93). Furthermore, the kernel associated with $\tilde{\mathcal{I}}_P^F$, $\tilde{\mathcal{I}}_P^S$ and $\tilde{\mathcal{I}}_\sigma^S$ is the same, so that both r.h.s terms of (40) share the same kernel respectively applied to the pressure and the axial stress. The very same feature is satisfied by the r.h.s of (90). Hence, the visco-elastic rheological based model (39)-(41) is similar with Keramat et al. (2011) (88)-(91) when using the $\tilde{\nu}_s = 1$ and $\alpha \to 0$ hypothesis. In other words, in the limit of thin-wall and without visco-elastic contribution to the

Poisson coupling, the proposed rheological model produces convolution kernels directly provided by the creep function, as previously done in [13, 28]. The various visco-elastic convolution kernels are compared in Figure 3 for the experimental data of [13] presented in Table 2. Each kernel family has been fitted with the same pressure field time variation coming from [19, 13]. Even though they present similar exponential decay family types, $\tilde{\mathcal{I}}_{Cov}$ and $\tilde{\mathcal{I}}_{Ker}$ display faster attenuation that the various kernels $\mathcal{I}_P^F, \mathcal{I}_\sigma^F, \mathcal{I}_P^S, \mathcal{I}_\sigma^S$ of the proposed model. Also, both $\mathcal{I}_P^F$ and $\mathcal{I}_\sigma^S$ are very similar for the obtained visco-elastic parameters.

Concerning the velocity dispersivity prediction provided in figure 4, it is interesting to mention that every models display a similar trend for the norm of complex velocities: it varies from a minimum value at $\omega = 0$ within a narrow low-frequency region (associated with a long time behaviour) so as to reach a constant plateau for large $|\omega|$ values. Hence, at short-time/large $|\omega|$ most dispersivity of the wave velocity is lost and the visco-elastic response is very much like the elastic one, [51, 52]. This allows to define a 'dispersive' frequency gap band depicted within vertical orange dotted lines for which visco-elastic effects are important. The 'dispersive' frequency gap band $\Delta\omega_v$ is more precisely define as the 95% difference velocity region from the asymptotic high-frequency regime, as exemplified in the inset of figure 4a. The larger this dispersive gap-band, and the deeper the $\omega = 0$ velocity, the larger visco-elastic effects are. It is interesting to observe in figure 4 that the dispersive gap is wider for Covas et al. [13] and Keramat et al. [28] models than for the hereby model (in black) for parameters obtained from the same data set [19, 13]. Considering specifically the corrective visco-elastic velocity $\tilde{c}_p^v(\omega)$ predictions analysed in figure 4a it can be observed that for the Covas [13] and Keramat [28] models the corrective visco-elastic velocity $\tilde{c}_p^v(\omega)$ tends to one in the $|\omega| \gg 1$ limit. Noteworthy, this is not the case for our model for which the high-frequency limit of $\tilde{c}_p^v(\omega)$ is approximately 6.5% above one as can be observed in figure 4a. Combining this limit with the $\tilde{c}_- \to 1$ as $|\omega| \gg 1$ found in figure 4c produces a slight over-visco-elastic-velocity of about 6.5% larger than the elastic one. These additional contributions to the elastic velocity from visco-elastic effects result from local terms in the visco-elastic kernels (as previously mentioned at the end of S.4.1.1). The vertical dotted line, depicted in the zoom inset of Figure 4a, reports the time-scale range for which the complex corrective velocity factor $\tilde{c}_p^v$ evaluated with the same visco-elastic parameter display a non-dissipative behaviour, i.e very weakly depends on frequency. This result is interesting per-see since it affects the predicted Joukowsky over-pressure which should be higher in visco-elastic materials when taking into account their elastic properties only. This 6.5% over-velocity of our prediction compared to Covas et al. [13] and Keramat et al. [28] models is also observable for $\tilde{c}_+$ in figure 4c. Previous studies, e.g. [19, 43, 20], had indeed pointed-out some difficulties in correctly estimating the effective wave speed in visco-elastic materials, consequently, leading to bad predictions for the first pressure overshoot according to Joukowsky's theory. The visco-elastic wave-speed correction (approximately evaluated between $10\% - 25\%$ in [19, 43, 20]) is of practical consequence. It should be taken into account in the modelling from using rheology-based visco-elastic dispersive velocities such as (49) and (53). This can be implemented using the transfer matrix method [53] recently extended to visco-elastic materials [54]. Such theoretical method which is very useful for leakage detection in pipes [55, 56, 57], could suffer from an approximated wave speed modelling that our contribution might improve. For now, we did only compared subsequent quantities not easy to measure experimentally i.e. visco-elastic kernels and the dispersive velocities. It is nevertheless interesting to compare predictions for the pressure signature to [13] and [28] ones. This comparison is illustrate in Figure 5 for the pressure signal at the valve. Whilst Covas's model slightly overshoot its prediction for the first pressure mode, it succeeds in nicely capturing the second and third one as illustrated in figure 5a. In time-domain, this first frequency overshoot manifests itself from a

systematic over-pressure prediction at long times as illustrated in figures 5c and 5e although more markedly noted in the case associated with dimensionless distance $Z = 0.42$. For these long-time behavior the proposed visco-elastic model in blue provides a better fit to the pressure dynamics. Nevertheless, at small time, the opposite can be observed in figure 5c for capturing the first peak. A similar behavior is observed with Keramat's model in 5b with an overshoot prediction for the first Fourier's peak, but for a less accurate fitting for the further second and third peaks. In time-domain, this again explains why Keramat's model over-predicts the pressure at long-time. It is interesting to observe that, at short time, both Keramat's model and the proposed visco-elastic one nicely match together, especially for providing high-frequency peaks which are absent in Covas's model prediction in figure 5a. These high-frequency peaks result from the FSI interaction from bouncing elastic waves in the solid obviously not considered in Covas's model. They are not observed in the experiments from high-frequency filtering of the measurement's sensors. Also of interest in figure 5a and 5b are the reported dispersive frequency band $\Delta\omega$ evaluated in figure 4a indicating which frequency range is associated with the elastic response (on the left) and the visco-elastic one (on the right). Overall our proposed visco-elastic model provides a convincing comparison to the pressure signal measured at various positions, comparable with other previous models.

4.6. Sensitivity analysis

This section considers the sensitivity analysis of visco-elastic kernels to parameters in the four-dimensional parameter-space of $(a, \tau_r, \tau_\lambda, \tau_\mu)$ –in general the elastic parameters (λ_e, μ_e) are supposed known material properties–. More precisely, any method (e.g. steepest-descent, Newton method, etc..) for minimizing the distance/the error between measurements and model's predictions needs the evaluation of visco-elastic kernel gradients in the parameter space. It is interesting to mention that the analytical relations between kernels $\tilde{\mathcal{I}}_P^F, \tilde{\mathcal{I}}_\sigma^F, \tilde{\mathcal{I}}_P^S, \tilde{\mathcal{I}}_\sigma^S$ and parameters $(a, \tau_r, \tau_\lambda, \tau_\mu)$ has been obtained in 64-67, permitting the explicit analytical evaluation of the kernel's Jacobian in parameter space if needed.

In order to simplify the picture, it is first interesting to realize from the definition of the visco-elastic kernels $\tilde{\mathcal{I}}_P^F, \tilde{\mathcal{I}}_\sigma^F, \tilde{\mathcal{I}}_P^S, \tilde{\mathcal{I}}_\sigma^S$ in 64-67 that these kernels are all linear functions of parameter a and τ_r. Thus the derivative of visco-elastic kernels in the $a - \tau_r$ space does not depend on these parameters and decays in time as illustrated in figures 6a and 6b. Considering the other parameters (τ_λ, τ_μ) being chosen at their optimal value, it is interesting to observe that the kernel derivatives in the $a - \tau_r$ sub-space is very moderate. In other words, visco-elastic kernels are poorly sensitive to a and τ_r parameters. Similarly the derivative of the kernels with respect to τ_λ are also moderate, with a significant decay in time, as illustrated in figure 7a -7d. On the contrary, the derivative of the kernels with respect to τ_μ reach much higher values as shown in figures 8a-8d where, at short time, the kernels derivatives are an order of magnitude more sensitive to τ_μ that all other parameters. Hence, from the four dimensional parameters, the most sensitive one to visco-elastic kernels is τ_μ, meaning that its precise evaluation is of clear significance in the parametric estimation. This result is consistent with the fact that the visco-elastic kernels exponential decay are directly related to τ_μ in (64)-(67).

5. Conclusion

A rheology-based model for water-hammer wave propagation in a visco-elastic pipe has been proposed. Using a long wavelength analysis and a generalized frequency-dependent Hooke-law for the stress/strain relation the pressure/longitudinal stress coupled wave system has been derived.

In this general framework, a visco-elastic FSI four equations model having four visco-elastic kernels and the corresponding pressure/longitudinal stress wave equation system have been established. This has first permitted us to find the generalized visco-elastic dispersive propagating velocity as explicit functions of the visco-elastic kernels. For a general linear visco-elastic rheology, the four visco-elastic kernels, and the corresponding creep function have been derived explicitly. They can be used to find visco-elastic rheology parameters in any specific pipe/boundary conditions configuration (e.g. from numerically solving the corresponding FSI-four equation problem, i.e. using a time-domain version of (39)-(41), with kernels (68)-(71) and creep function (63)). Furthermore, for specific boundary conditions, an explicit analytical solution in Fourier domain for the pressure/stress wave has been derived and used so as to estimate the visco-elastic parameters from experimental water-hammer time-domain pressure measurements from numerical inverse Fourier transform.

The model's predictions have then been successfully compared to the experimental measurements as well as with other models adjusted to the same experimental data set. Also, the model's parameter sensitivity has been quantified by computing the four visco-elastic kernels derivative with parameters, showing a stronger influence of the viscous relaxation time τ_μ over all other parameters. This contribution has shown that the proposed rheology-based visco-elastic model provides a convincing description of the water-hammer wave propagation in the visco-elastic pipe. It can be used in many other contexts with the specific ability to distinguish the intrinsic visco-elastic rheology from the considered pipe geometry and boundary conditions.

Let us finally discuss the practical relevance and usefulness of this contribution. Even if the proposed model needs parameter calibration exactly as previous other visco-elastic Kelvin-Voigt models, it nevertheless presents two distinct features. First, as opposed to other models which need the numerical computation of the water-hammer wave system problem, our Fourier-domain analytical solution permits getting the time-domain pressure solution from a simple Fourier transform only. This is more simple and more useful than being able to accurately compute the wave equations (a hyperbolic problem necessitates devoted numerical schemes and methods). Furthermore, the minimisation between observation and model for parameter calibration could also be performed in frequency-domain, from a simple Fourier transform of the pressure observations themselves as done in this paper in Figures 5a and 5b. In this case, the parameter calibration could directly benefit from our analytical solution as well as from the analytical sensitivity matrix computation, the derivative of which is needed in the calibration numerical procedure. This is a simplified procedure over the state of the art. Secondly, because our parameters are rheology-based, they can be estimated before-end from applied mechanical stress-strain response tests. These mechanical stress-strain tests might be of various kinds (e.g. oscillatory, shear, compression, mixed, etc..) so as to increase the parameter estimation step robustness. In this case, the presented model could provide water-hammer time-domain pressure prediction without the need for parameter calibration on water-hammer tests. A distinct path which is beyond the scope of the present paper but might motivate future investigations.

Acknowledgement

This work is under a CC-BY 4.0 licence. This work was supported by the collaborative ANRT Grant CIFRE 2019/1453 co-funded by SETOM, a dedicated society of Veolia for the public drinking water service of Toulouse Métropole operating under the brand Eau de Toulouse Métropole. The authors thank Pr. D. Covas from Lisbon University for sharing her data on visco-elastic damped waves.

The authors have no competing interests to declare.

References

[1] A. S. Tijsseling, Fluid-Structure Interaction in liquid-filled pipe systems: a review, J. Fluids Struct. 10 (2) (1996) 109–146.

[2] P. Flaud, D. Geiger, C. Oddou, D. Quemada, Ecoulements pulsés dans les tuyaux visco-élastiques. application à l'étude de la circulation sanguine., J. de Physique 35 (1974) 869–882.

[3] S. Čanić, J. Tambača, G. Guidoboni, A. Mikelić, C. J. Hartley, D. Rosenstrauch, Modeling Viscoelastic Behavior of Arterial Walls and Their Interaction with Pulsatile Blood Flow, SIAM J. Appl. Math. 67 (1) (2006) 164–193, publisher: Society for Industrial and Applied Mathematics.

[4] D. Bessems, C. Giannopapa, M. Rutten, F. Van De Vosse, Experimental validation of a time-domain-based wave propagation model of blood flow in viscoelastic vessels, J. Biomech. 41 (2) (2008) 284–291.

[5] N. Duraiswamy, R. T. Schoephoerster, M. R. Moreno, J. E. Moore, Jr., Stented artery flow patterns and their effects on the artery wall, Annu. Rev. Fluid Mech. 39 (2007) 357–382.

[6] F. N. Van De Vosse, N. Stergiopulos, Pulse wave propagation in the arterial tree, Annu. Rev. Fluid Mech. 43 (2011) 467–499.

[7] E. Rieutord, A. Blanchard, Influence d'un comportement viscoélastique de la conduite dans le phénomène du coup de bélier, C. R. Acad. Sci. 274 (1972) 1963–1966.

[8] M. Gally, M. Güney, E. Rieutord, An investigation of pressure transients in viscoelastic pipes, J. Fluids Eng. 101 (4) (1979) 495–499.

[9] E. Rieutord, A. Blanchard, Pulsating viscoelastic pipe flow - water-hammer, J. Hydraul. Res. 17 (3) (1979) 217–229.

[10] G. Kuiken, Wave propagation in a thin-walled liquid-filled initially-stressed tube, J. Fluid Mech. 141 (1984) 289–308.

[11] R. P. Sawatzky, M. B., On the propagation of pressure pulses through a viscous fluid contained in a visco-elastic tube, Q. J. Mech. Apppl. Math. 41 (1) (1988) 33–50.

[12] L. Suo, E. B. Wylie, Complex Wavespeed and Hydraulic Transients in Viscoelastic Pipes, J. Fluid Eng. 112 (4) (1990) 496–500.

[13] D. Covas, I. Stoianov, J. F. Mano, H. Ramos, N. Graham, C. Maksimovic, The dynamic effect of pipe-wall viscoelasticity in hydraulic transients. Part II model development, calibration and verification, J. Hydraul. Res. 43 (1) (2005) 56–70.

[14] H. Ramos, D. Covas, A. Borga, D. Loureiro, Surge damping analysis in pipe systems: modelling and experiments, J. Hydraul. Res. 42 (4) (2004) 413–425.

[15] N. Kizilova, Pressure Wave Propagation in Liquid-Filled Tubes of Viscoelastic Material, Fluid Dyn. 41 (2006) 434–446.

[16] C. C. Mei, H. Jing, Pressure and wall shear stress in blood hammer – Analytical theory, Math. Biosci. 280 (2016) 62–70.

[17] A. Bayle, F. Plouraboué, Low–mach number asymptotic analysis of Fluid–Structure-Interaction (FSI) pressure waves inside an elastic tube, Eur. J. Mech. B Fluids (2023). doi:https://doi.org/10.1016/j.euromechflu.2023.04.014.

[18] T. Khudayarov, Mathematical simulation of nonlinear oscillations of viscoelastic pipelines conveying fluid, Appl. Math 66 (2019) 662–679.

[19] D. Covas, I. Stoianov, H. Ramos, N. Graham, C. Maksimovic, The dynamic effect of pipe-wall viscoelasticity in hydraulic transients. Part I Experimental analysis and creep characterization, J. Hydraul. Res. 42 (2004) 517–532.

[20] K. Weinerowska-Bords, Viscoelastic Model of Waterhammer in Single Pipeline–Problems and Questions, Arch. Hydroengineering Environ. Mech. 53 (2006) 331–351.

[21] A. K. Soares, D. Covas, L. F. Reis, Analysis of PVC Pipe-Wall Viscoelasticity during Water Hammer, J. Hydraul. Eng. 134 (9) (Sep. 2008).

[22] S. Meniconi, B. Brunone, M. Ferrante, Water-hammer pressure waves interaction at cross-section changes in series in viscoelastic pipes, J. Fluids Struct. 33 (2012) 44–58.

[23] K. Urbanowicz, M. Firkowski, Z. Zarzycki, Modelling water hammer in viscoelastic pipelines: short brief, J. Phys. Conf. Ser. 760 (2016) 012037.

[24] K. Urbanowicz, D. Huan-Feng, A. Bergant, Transient flow of liquid in plastic pipes, J. Mech. Eng. Res. 66 (2) (2020) 77–90.

[25] Z. Duan, T. Li, Comprehensive application analyses of elastic models and viscoelastic models in transient flows in polymeric pipelines, J. Hydroinformatics 24 (5) (2022) 1020–1052.

[26] K. Weinerowska-Bords, Alternative approach to convolution term of viscoelasticity in equations of unsteady pipe flow, J. Fluids Eng. 137 (5) (2015) 054501.

[27] S. Li, B. W. Karney, G. Liu, FSI research in pipeline systems – A review of the literature, J. Fluids Struct. 57 (2015) 277–297.

[28] A. Keramat, A. Tijsseling, Q. Hou, A. Ahmadi, Fluid–structure interaction with pipe-wall viscoelasticity during water hammer, J. Fluids Struct. 28 (2011) 434–455.

[29] R. S. Hosseini, A. Ahmadi, R. Zanganeh, Fluid-structure interaction during water hammer in a pipeline with different performance mechanisms of viscoelastic supports, J. Sound Vib. 487 (2020) 115527.

[30] M. T. Shaw, W. J. MacKnight, Introduction to polymer viscoelasticity, 4^{th} edition, John Wiley & Sons, 2018.

[31] A. Monteiro, F. B. Freitas Rachid, A. Tijsseling, Fluid transients in viscoelastic pipes via an internal variable constitutive theory, Appl. Math 114 (2023) 846–869.

[32] D. Covas, I. Stoianov, H. Ramos, N. G., C. Maksimović, D. Butler, Water hammer in pressurized polyethylene pipes: conceptual model and experimental analysis, Urban Water J. 1 (2) (2004) 177–197.

[33] G. Pezinga, B. Brunone, M. S., Relevance of Pipe Period on Kelvin-Voigt Viscoelastic Parameters : 1d and 2d Inverse Transient Analysis, J. Hydraul. Eng. 142 (12) (2016) 04016063.

[34] A. Tijsseling, Water hammer with fluid-structure interaction in thick-walled pipes, Comput. Struct. 85 (2007) 844–851.

[35] A. Bayle, F. Plouraboué, Spectral properties of Fluid Structure Interaction pressure/stress waves in liquid filled pipes, Wave motion 116 (2023) 103081.

[36] J. Massey, B. S.; Ward-Smith, Mechanics of Fluids, 7th ed. Cheltenham: Nelson Thornes, 1998.

[37] N. Joukowski, Über den hydraulischen stoss in wasserleitungsröhren, Mémoires de l'Académie Impériale des Sciences de St.-Pétersbourg 8 (9(5)) (1900) 1–71.

[38] N. Joukowski, , t. b. O. Simin, Memoirs of the imperial academy society of St.-Petersburg, Proc. Amer. Water Works Assoc. 24 (1904) 341–424.

[39] R. Skalak, An extension of the theory of waterhammer, J. Fluids Eng. Trans. ASME 78 (1956) 105–116.

[40] T. Lin, G. W. Morgan, Wave propagation through fluid contained in a cylindrical, elastic shell, J. Acoust. Soc. Am. 28 (1956) 1165–1176.

[41] J. S. Walker, J. W. Phillips, Pulse Propagation in Fluid-Filled Tubes, J. Appl. Mech. 44 (1) (1977) 31–35.

[42] A. E. H. Love, A treatise on the mathematical theory of elasticity., Dover, 1944.

[43] M. Mitosek, M. Chorzelski, Influence of visco-elasticity on pressure wave velocity in polyethylene MDPE pipe, Arch. Hydroengineering Environ. Mech. Vol. 50 (2) (2003) 127–140.

[44] J. M. Carcione, F. Poletto, D. Gei, 3-D wave simulation in anelastic media using the Kelvin–Voigt constitutive equation, J. Comput. Phys. 196 (1) (2004) 282–297.

[45] A. Eringen, Mechanics of Continua, R. E. Krieger Publishing Company, 1980.

[46] D. Bland, The Theory of Linear Viscoelasticity, Dover Books on Physics, Dover Publications, 2016.

[47] D. Annie, On a Theory of Thermoviscoelastic Materials with Voids, J. Elast. 104 (2011) 369–384.

[48] J. Sharma, M. I. Othman, Effect of rotation on generalized thermo-viscoelastic Rayleigh–Lamb waves, Int. J. Solids Struct. 44 (13) (2007) 4243–4255.

[49] M. S. Ghidaoui, M. Zhao, D. A. McInnis, D. H. Axworthy, A review of water hammer theory and practice 58 (1) (2005) 49–76. doi:10.1115/1.1828050.

[50] J. Gong, A. C. Zecchin, M. F. Lambert, A. R. Simpson, Determination of the Creep Function of Viscoelastic Pipelines Using System Resonant Frequencies with Hydraulic Transient Analysis, J. Hydraul. Eng. 142 (9) (2016) 04016023.

[51] F. Barez, W. Goldsmith, J. L. Sackman, Longitudinal waves in liquid-filled tubes—I: Theory, Int. J. Mech. Sci. 21 (4) (1979) 213–221.

[52] M. Prek, Analysis of wave propagation in fluid-filled viscoelastic pipes, Mech Syst Signal Process 21 (2007) 1907–1916.

[53] L. Zhang, A. Tijsseling, E. Vardy, FSI Analysis of Liquid-Filled Pipes, J. Sound Vib. 224 (1999) 69–99.

[54] H. K. Aliabadi, A. Ahmadi, A. Keramat, Frequency response of water hammer with fluid-structure interaction in a viscoelastic pipe, Mech Syst Signal Process 144 (2020) 106848.

[55] A. Keramat, H.-F. Duan, Spectral based pipeline leak detection using a single spatial measurement, Mech Syst Signal Process 161 (2021) 107940.

[56] A. Keramat, B. Karney, M. S. Ghidaoui, X. Wang, Transient-based leak detection in the frequency domain considering fluid-structure interaction and viscoelasticity, Mech Syst Signal Process 153 (2021) 107500.

[57] X. Wang, G. A. Camino, T.-C. Che, M. S. Ghidaoui, Factorized wave propagation model in tree-type pipe networks and its application to leak localization, Mech Syst Signal Process 147 (2021) 107116.

[58] F. Khan, C. Yeakle, Experimental investigation and modeling of non-monotonic creep behavior in polymers, Int. J. Plast. 27 (4) (2011) 512–521.

[59] E. Kontou, S. Katsourinis, Application of a fractional model for simulation of the viscoelastic functions of polymers, J. Appl. Polym. Sci. 133 (23) (2016).

[60] S. Neidigk, C. Salas, E. Soliman, D. Mercer, M. Reda Taha, Creep and relaxation of osteoporotic bones, in: Society for Experimental Mechanics - SEM Annual Conference and Exposition on Experimental and Applied Mechanics 2009, Vol. 4, 2009, pp. 1–4.

Appendix A. Visco-elastic parameters estimation from creep and stress relaxation methods

In this appendix, the rheological parameters identification within a 3D linear rheological model is discussed. Most common rheological models are based upon a mechanical approach, where springs and dashpot are associated in order to establish differential equations describing media's deformation. The Kelvin-Voigt, Maxwell, and Zener models are built within this approach and represent 1D models involving parameters either directly fitted to pressure signals [32, 28] or to mechanical measurements [58, 59]. A wide variety of techniques (e.g. creep and stress relaxation, free oscillation methods, resonance methods, and wave propagation methods) based on different solicitation frequencies can be used to quantify visco-elastic models and estimate their parameters.

Here, the details of the rheological parameters determination of 3D models 59 based on the creep and stress relaxation methods are presented. In index form model 59 reads

$$a(1+\tau_r\partial_t)\sigma^*_{ij} = \lambda_e(1+\tau_\lambda\partial_t)\epsilon^*_{ll}\delta_{ij} + 2\mu_e(1+\tau_\mu\partial_t)\epsilon^*_{ij}, \tag{A.1}$$

δ_{ij} being the Kronecker's symbol. In rheological studies, one applies stress (either constant or oscillating) to the visco-elastic media and measures the associated strain. Hence, the strain field components ϵ^*_{ij}, have to be written versus the stress fields ones σ^*_{ij}, thus inverting (A.1). Let us first focus on the non-diagonal part of (A.1). The strain non-diagonal components achieve as follows

$$\epsilon^*_{ij}(t) = \frac{1}{2\mu_e}\,\frac{a}{\tau_\mu}\int_0^t (1+\tau_r\partial_T)\sigma^*_{ij}(T)\; e^{\frac{T-t}{\tau_\mu}}\; dT + \epsilon^*_{ij}(0)\; e^{-t/\tau_\mu}, \tag{A.2}$$

whilst performing an integration by parts of (A.2)'s r.h.s, yields

$$\epsilon^*_{ij}(t) = \underbrace{\frac{a}{2\mu_e}\;\left(1-\frac{\tau_r}{\tau_\mu}\right)\frac{1}{\tau_\mu}\int_0^t \sigma^*_{ij}(T)e^{\frac{T-t}{\tau_\mu}}\; dT}_{\text{Visco-elastic component}} + \underbrace{\frac{\tau_r}{\tau_\mu}\frac{a}{2\mu_e}\sigma^*_{ij}(t)}_{\text{Elastic component}} + \underbrace{\left(\epsilon^*_{ij}(0) - \frac{\tau_r}{\tau_\mu}\frac{a}{2\mu_e}\sigma_{ij}(0)\right)}_{\text{Initial conditions}}\; e^{-t/\tau_\mu}. \tag{A.3}$$

The ϵ^*_{ij} strain field components are therefore composed of three terms. A visco-elastic component whose dynamics is only driven by the characteristic shear-time τ_μ, an elastic component whose response is instantaneous and an exponentially decaying initial conditions contribution. The inversion of (A.1)'s diagonal terms is now considered. Introducing the stress $\boldsymbol{\sigma}^*_d$ and strain $\boldsymbol{\epsilon}^*_d$ vector field

$$\boldsymbol{\sigma}^*_d = \left(\sigma^*_{xx}(t), \sigma^*_{yy}(t), \sigma^*_{zz}(t)\right)^T \quad \text{, and } \quad \boldsymbol{\epsilon}^*_d = \left(\epsilon^*_{xx}(t), \epsilon^*_{yy}(t), \epsilon^*_{zz}(t)\right)^T. \tag{A.4}$$

From considering the applied stress configurations of figure A.9b, it yields

$$\lambda_e\;\left[\tau_\lambda\partial_t + \mathbf{A^{-1}B}\right]\boldsymbol{\epsilon}^*_d = a\mathbf{A}^{-1}\left(1+\tau_r\partial_t\right)\boldsymbol{\sigma}^*_d, \tag{A.5}$$

with $\mathbf{A}$ and $\mathbf{B}$ defined by

$$\mathbf{A} = \begin{pmatrix} 1+\frac{\mu_e}{\lambda_e}\frac{\tau_\mu}{\tau_\lambda} & 1 & 1 \\ 1 & 1+\frac{\mu_e}{\lambda_e}\frac{\tau_\mu}{\tau_\lambda} & 1 \\ 1 & 1 & 1+\frac{\mu_e}{\lambda_e}\frac{\tau_\mu}{\tau_\lambda} \end{pmatrix} \quad \text{, and, } \quad \mathbf{B} = \begin{pmatrix} 1+2\frac{\mu_e}{\lambda_e} & 1 & 1 \\ 1 & 1+2\frac{\mu_e}{\lambda_e} & 1 \\ 1 & 1 & 1+2\frac{\mu_e}{\lambda_e} \end{pmatrix}. \tag{A.6}$$

To obtain the strain evolution, $\mathbf{A^{-1}B}$ is diagonalized. In the eigenvector basis, it follows

$$\left(\partial_t + \boldsymbol{\Omega}\right)\hat{\boldsymbol{\epsilon}}^*_d = \frac{a(1+\nu_e)}{E_e}\;\; \mathbf{F}\;\; \left(1+\tau_r\partial_t\right)\hat{\boldsymbol{\sigma}}^*_d, \tag{A.7}$$

with $\boldsymbol{\Omega}$ and $\mathbf{F}$ defined by

$$\boldsymbol{\Omega} = \begin{pmatrix} 1/\tau_\mu & 0 & 0 \\ 0 & 1/\tau_\mu & 0 \\ 0 & 0 & 1/\tau_E \end{pmatrix} \quad \text{, and, } \quad \mathbf{F} = \begin{pmatrix} 1/\tau_\mu & 0 & 0 \\ 0 & 1/\tau_\mu & 0 \\ 0 & 0 & \frac{1}{\tau_E}\;\frac{1-2\nu_e}{1+\nu_e} \end{pmatrix}, \tag{A.8}$$

whilst $\hat{\boldsymbol{\epsilon}}_d$ and $\hat{\boldsymbol{\sigma}}_d$ vectors are defined by

$$\boldsymbol{\epsilon}_d^* = \mathbf{\Pi}\ \hat{\boldsymbol{\epsilon}}_{\mathbf{d}}^* \ \text{, and, } \ \boldsymbol{\sigma}_{\mathbf{d}}^* = \mathbf{\Pi}\ \hat{\boldsymbol{\sigma}}_{\mathbf{d}}^* \ \text{, where } \ \mathbf{\Pi} = \begin{pmatrix} -1 & -1 & 1 \\ 0 & 1 & 1 \\ 1 & 0 & 1 \end{pmatrix}. \tag{A.9}$$

Using the base change matrix $\mathbf{\Pi}$, we found the strain components as

$$\begin{aligned} \epsilon_i^*(t) =& \frac{a(1+\nu_e)}{E_e} \left[\underbrace{\int_0^t \sum_j \Pi_{ij} F_{jj} \hat{\sigma_j}^*(T)\ e^{(T-t)\Omega_{jj}}\ (1-\tau_r\Omega_{jj}) dT}_{\text{Visco-elastic component}} + \underbrace{\sum_j \tau_r \Pi_{ij} F_{jj} \hat{\sigma_j}^*(t)}_{\text{Elastic component}} \right] \\ &+ \underbrace{\sum_j \Pi_{ij} \left(\hat{\epsilon_i}^*(0) - \frac{(1+\nu_e)}{E_e} \hat{\sigma_j}^*(0) \right) e^{-t\Omega_{jj}}}_{\text{Initial conditions}}. \end{aligned} \tag{A.10}$$

Similarly to the shear case, the strain field can be expressed with three contributions: (i) a visco-elastic one the dynamics of which is driven by the characteristic times resulting from matrix $\mathbf{\Omega}$ and $\mathbf{F}$ (ii) an elastic one, not depending of time, having an instantaneous contribution (iii) an exponentially decaying initial conditions contribution, the characteristic time of which results from matrix $\mathbf{\Omega}$. Using the model previously developed in the context of stress or creep relaxation tests, it is possible to determine parameters $(a, \tau_r, \tau_\mu, \tau_\lambda)$ for various visco-elastic materials. Unfortunately, all model's parameters cannot be determined through a single experiment. Indeed, for a creep test, the characteristic stress relaxation time τ_r does not appear. It is, therefore, necessary to carry out two independent tests, a creep one and a stress relaxation one so as to determine all model parameters. However, for a given material it is not easy to find all the necessary mechanical stress configurations in the literature to close the parameter estimations. We perform some of those from the data sets found in the literature to further exemplified the approach.

Appendix A.1. Creep

In the framework of a single step loading of a stress σ_0^*, the model predicts the strain from (A.10), so that the creep compliance $J^*(t) = \epsilon^*(t)/\sigma_0^*$ is

$$J^*(t) = J^*(0) \left[a - \frac{1-a}{3} \left(2(1+\nu_e) e^{-t/\tau_\mu} + (1-2\nu_e) e^{-t/\tau_E} \right) \right]. \tag{A.11}$$

This test allows to determine parameters $(a, \tau_\mu, \tau_\lambda)$.

Appendix A.2. Stress relaxation

Similarly to the creep test, for a single step strain ϵ_0^*, the model involves stress from (A.3) and therefore Young modulus $E_{(t)} = \sigma^*(t)/\epsilon_0^*$

$$E(t) = \frac{E_e}{a} \left(1 + (a-1) e^{-at/\tau_r} \right). \tag{A.12}$$

This test allows finding parameters (a, τ_r). Note that in both experiments, the a value can be evaluated, thus providing a cross-checked evaluation.
An example of parameter estimation based on creep and stress relaxation tests on femur bones experiments carried out by [60] is illustrated inA.10. The parameter estimation has been carried out using a least square method in order to find the minimum error between the model and data. Figure A.10 display the stress and strain time variations respectively associated with stress relaxation and creep tests. Parameters $a = 1.77$ and $\tau_r = 4.42h$ for the stress relaxation test and $a = 1.41$, $\tau_\mu = 4.32\ min$ and $\tau_\lambda = 33.8\ min$ for the creep test have been found. These results show a good agreement between the model with the experimental measurements. Also, the a value estimate lies within the 25% difference between both tests. The a parameter is then allowed to characterize the visco-elastic strain of a material, which is added to its elastic strain. It is thus necessarily larger than one. Furthermore the larger parameter a, the more visco-elastic the media.

Appendix B. Theoretical derivation of the visco-elastic FSI four-equations model

Keeping $O(1)$ terms and neglecting $O(\epsilon^2)$ in (29)-(30), it is possible to find that, to leading order, the displacements fields fulfils (Cf [35] for more details)

$$\tilde{\zeta} = \tilde{H}_1(Z,\omega) \quad \text{, and, } \quad \tilde{\xi} = \frac{\tilde{H}_2(Z,\omega)}{2} R + \frac{\tilde{H}_3(Z,\omega)}{R}, \tag{B.1}$$

where $\tilde{H}_{[1,2,3]}$ are functions of ω and Z given by the boundary conditions associated with axial velocity and radial constraint (Cf [35]). Note that this analysis is a long wavelength approach which neglects $O(\epsilon^2)$ (Cf [17] for more details on the asymptotic context) so that (B.1) is in fact consistent with (26). Following [35], combining boundary conditions (35)-(36) with $\tilde{\xi}$ expression in (B.1) whilst using visco-elastic Poisson modulus (8) and (11) leads to

$$\tilde{H}_2(Z,\omega) = 2\nu_e \tilde{\nu}_s(\omega) \left(\tilde{\mathcal{C}}_{\lambda_s}(\omega) \frac{\tilde{P}}{\alpha^2(2+\alpha)} - \partial_Z \tilde{\zeta} \right) \quad \text{, and, } \quad \tilde{H}_3(Z,\omega) = \tilde{\mathcal{C}}_{\mu_s}(\omega) \frac{(1+\alpha)^2}{2\alpha^2(2+\alpha)} \tilde{P}. \tag{B.2}$$

The deformation vector field at the solid wall is necessary in order to close fluid momentum equation (33). It can be found from replacing results (B.2) in (B.1)

$$\tilde{\xi}\big|_{R=1} = \frac{\tilde{\chi}_s(\omega)\tilde{P}}{2\alpha} - \nu_e \tilde{\nu}_s(\omega) \partial_Z \tilde{\zeta}, \tag{B.3}$$

$$\tilde{\chi}_s(\omega) = \frac{2\nu_e \tilde{\nu}_s(\omega) \tilde{\mathcal{C}}_{\lambda_s}(\omega) + (1+\alpha)^2 \tilde{\mathcal{C}}_{\mu_s}(\omega)}{\alpha(2+\alpha)} \tag{B.4}$$

where $\tilde{\chi}_s(\omega)$ generalizes the elastic effective velocity parameters χ_e, introduced in (1). Now, considering the leading-order solid stress, from $\tilde{\sigma}_{rz}$ in (28), whilst using (B.1) as well as $\tilde{\sigma}_{zz}$ in (25), the shear-stress boundary conditions (35)-(36) leads to find zero shear-stress everywhere inside the solid (at leading order, neglecting $O(\epsilon^2)$), as in the elastic case [34, 35]

$$\tilde{\sigma}_{rz} = 0. \tag{B.5}$$

It is noteworthy that this zero-shear stress in the solid is also a hypothesis of thin-shell approximation, hence consistent with this result. Using (B.2) in (B.1) to replace the $\tilde{\xi}$ field in the axial

constraint $\tilde{\sigma}_{zz}$ visco-elastic rheology expression (25) yields

$$\tilde{\sigma}_{zz} = 2\nu_e\tilde{\nu}_s\frac{\tilde{P}}{\alpha(2+\alpha)} + \frac{\alpha\tilde{\mathcal{C}}_s^2}{\mathcal{D}}\partial_Z\tilde{\zeta}, \tag{B.6}$$

whilst simplification $\alpha\left[\frac{2}{\tilde{\mathcal{C}}_{\mu_s}} + \frac{1-2\nu_e\tilde{\nu}_s}{\tilde{\mathcal{C}}_{\lambda_s}}\right] \equiv \frac{\alpha\tilde{\mathcal{C}}_s^2}{\mathcal{D}}$ has also been used. Finally, combining (28) and (B.5), one gets

$$\frac{\alpha}{\mathcal{D}}\omega^2\tilde{\zeta} + \partial_Z\tilde{\sigma}_{zz} = 0. \tag{B.7}$$

By, using (33), (34), (B.3), (B.6) and (B.7), the dimensionless visco-elastic FSI four equation model can be derived

$$\begin{aligned}
i\omega\tilde{W} &= -\partial_Z\tilde{P} && \text{(B.8)}\\
i\omega\tilde{P} + \mathcal{C}^2\partial_Z\tilde{W} &= -i\omega\mathcal{C}^2\left[\tilde{\chi}_s\tilde{P} - 2\alpha\nu_e\tilde{\nu}_s\partial_Z\tilde{\zeta}\right], && \text{(B.9)}\\
\tilde{\sigma}_{zz} &= 2\nu_e\tilde{\nu}_s\frac{\tilde{P}}{\alpha(2+\alpha)} + \frac{\alpha\tilde{\mathcal{C}}_s^2}{\mathcal{D}}\partial_Z\tilde{\zeta}, && \text{(B.10)}\\
\frac{\alpha}{\mathcal{D}}\omega^2\tilde{\zeta} + \partial_Z\tilde{\sigma}_{zz} &= 0. && \text{(B.11)}
\end{aligned}$$

Injecting (B.10) in (B.9) permits to express the r.h.s of (B.9) versus pressure and axial stress, i.e.

$$i\omega\tilde{P} + \partial_Z\tilde{W} - 2\alpha i\omega\nu_e\partial_Z\tilde{\zeta} = -i\omega\left[\left(\tilde{\chi}_s - \chi_e + \frac{4\nu_e^2\tilde{\nu}_s\left(\tilde{\nu}_s-1\right)\mathcal{D}}{\alpha(2+\alpha)\tilde{\mathcal{C}}_s^2}\right)\tilde{P} - 2\mathcal{D}\frac{\nu_s^e\left(\tilde{\nu}_s-1\right)}{\tilde{\mathcal{C}}_s^2}\tilde{\sigma}_{zz}\right], \tag{B.12}$$

or equivalently

$$i\omega\tilde{P} + \partial_Z\tilde{W} - 2\alpha i\omega\nu_e\partial_Z\tilde{\zeta} = -i\omega\left[\chi_e\left(\frac{\tilde{\chi}_s - \chi_e}{\chi_e} + \frac{4\nu_e^2\tilde{\nu}_s\left(\tilde{\nu}_s-1\right)\mathcal{D}}{\alpha(2+\alpha)\chi_e\tilde{\mathcal{C}}_s^2}\right)\tilde{P} - 2\mathcal{D}\frac{\nu_e\left(\tilde{\nu}_s-1\right)}{\tilde{\mathcal{C}}_s^2}\tilde{\sigma}_{zz}\right]. \tag{B.13}$$

The elastic and visco-elastic velocity parameters $(\chi_e, \tilde{\chi}_s)$ introduced in (1) and (B.4) respectively, can be revised regarding the solid acoustic wave speeds (13), their ratio to the acoustic fluid wave speed (14) and the density ratio (18). It thus follows

$$\begin{aligned}
\chi_e &= \frac{4\mathcal{D}}{\alpha(2+\alpha)\mathcal{C}_s^{e\,2}}\left[1 - \nu_e^2 + \frac{\alpha(2+\alpha)}{2}(1+\nu_s^e)\right], && \text{(B.14)}\\
\tilde{\chi}_s &= \frac{4\mathcal{D}}{\alpha(2+\alpha)\tilde{\mathcal{C}}_s^2}\left[1 - \nu_e^2\tilde{\nu_s}^2 + \frac{\alpha(2+\alpha)}{2}(1+\nu_e\tilde{\nu}_s)\right], && \text{(B.15)}
\end{aligned}$$

so as to achieve

$$\frac{\tilde{\chi}_s - \chi_e}{\chi_e} + \frac{4\nu_e^2\tilde{\nu}_s\left(\tilde{\nu}_s-1\right)\mathcal{D}}{\alpha(2+\alpha)\chi^e\tilde{\mathcal{C}}_s^2} = \left(\frac{\mathcal{C}_s^e}{\tilde{\mathcal{C}}_s}\right)^2\frac{1 - \nu_e^2\tilde{\nu}_s^2 + \frac{\alpha(2+\alpha)}{2}(1+\nu_e\tilde{\nu}_s^s) + \nu_e^2\tilde{\nu}_s(\tilde{\nu}_s-1)}{1 - \nu_e^2 + \frac{\alpha(2+\alpha)}{2}(1+\nu_e)} - 1, \tag{B.16}$$

or equivalently

$$\frac{\tilde{\chi}_s - \chi_e}{\chi_e} + \frac{4\nu_e^2\tilde{\nu}_s\left(\tilde{\nu}_s-1\right)\mathcal{D}}{\alpha(2+\alpha)\chi^e\tilde{\mathcal{C}}_s^2} = \left(\frac{\mathcal{C}_s^e}{\tilde{\mathcal{C}}_s}\right)^2\frac{1 - \nu_e^2\tilde{\nu}_s + \frac{\alpha(2+\alpha)}{2}(1+\nu_e\tilde{\nu}_s^s)}{1 - \nu_e^2 + \frac{\alpha(2+\alpha)}{2}(1+\nu_e)} - 1. \tag{B.17}$$

Finally, the relation (B.13) results in

$$i\omega\tilde{P}+\partial_Z\tilde{W}-2\alpha i\omega\nu_e\partial_Z\tilde{\zeta}=2\mathcal{D}i\omega\frac{\nu_e(\tilde{\nu}_s-1)}{\tilde{\mathcal{C}}_s^2}\tilde{\sigma}_{zz}-\chi_e i\omega\left(\left(\frac{\mathcal{C}_s^e}{\tilde{\mathcal{C}}_s}\right)^2\frac{\nu_e^2\tilde{\nu}_s-1-\frac{\alpha(2+\alpha)}{2}(1+\nu_e\tilde{\nu}_s^s)}{\nu_e^2-1-\frac{\alpha(2+\alpha)}{2}(1+\nu_e)}-1\right)\tilde{P}. \quad \text{(B.18)}$$

Likewise, the (B.10) r.h.s is modified to bring out elastic contributions in its l.h.s

$$\tilde{\sigma}_{zz}-2\nu_e\frac{\tilde{P}}{\alpha(2+\alpha)}-\frac{\alpha\mathcal{C}_s^{e2}}{\mathcal{D}}\partial_Z\tilde{\zeta}=2\nu_e\left(\tilde{\nu}_s-1\right)\frac{\tilde{P}}{\alpha(2+\alpha)}+\frac{\alpha}{\mathcal{D}}\left(\tilde{\mathcal{C}}_s^2-\mathcal{C}_s^{e2}\right)\partial_Z\tilde{\zeta}, \quad \text{(B.19)}$$

so that re-injecting the $\partial_Z\tilde{\zeta}$ term of (B.10) yields

$$\tilde{\sigma}_{zz}-2\nu_e\frac{\tilde{P}}{\alpha(2+\alpha)}-\frac{\alpha\mathcal{C}_s^{e2}}{\mathcal{D}}\partial_Z\tilde{\zeta}=\frac{\tilde{\mathcal{C}}_s^2-\mathcal{C}_s^{e2}}{\tilde{\mathcal{C}}_s^2}\tilde{\sigma}_{zz}+\frac{2\nu_e}{\alpha(2+\alpha)}\left(\tilde{\nu}_s-1-\tilde{\nu}_s\frac{\tilde{\mathcal{C}}_s^2-\mathcal{C}_s^{e2}}{\tilde{\mathcal{C}}_s^2}\right)\tilde{P}. \quad \text{(B.20)}$$

Finally, (B.8), (B.9),(B.18) and (B.10) lead to

$$\begin{aligned}
i\omega\tilde{W} &= -\partial_Z\tilde{P} && \text{(B.21)}\\
i\omega\tilde{P}+\partial_Z\tilde{W}-2i\omega\alpha\nu_e\partial_Z\tilde{\zeta} &= -i\omega\chi_e\tilde{\mathcal{I}}_P^F\tilde{P}+\frac{2\mathcal{D}\nu_e}{\mathcal{C}_s^{e2}}i\omega\tilde{\mathcal{I}}_\sigma^F\tilde{\sigma}_{zz}, && \text{(B.22)}\\
i\omega\tilde{\sigma}_{zz}-\frac{2\nu_e}{\alpha(2+\alpha)}i\omega\tilde{P}-i\omega\frac{\alpha\mathcal{C}_s^{e2}}{\mathcal{D}}\partial_Z\tilde{\zeta} &= -i\omega\tilde{\mathcal{I}}_\sigma^S\tilde{\sigma}_{zz}+\frac{2\nu_e}{\alpha(2+\alpha)}i\omega\tilde{\mathcal{I}}_P^S\tilde{P}, && \text{(B.23)}\\
\frac{\alpha}{\mathcal{D}}\omega^2\tilde{\zeta}+\partial_Z\tilde{\sigma}_{zz} &= 0, && \text{(B.24)}
\end{aligned}$$

where the hereby introduced visco-elastic extra terms $\tilde{\mathcal{I}}_P^F$, $\tilde{\mathcal{I}}_\sigma^F$, $\tilde{\mathcal{I}}_P^S$ and $\tilde{\mathcal{I}}_\sigma^S$ read

$$\begin{aligned}
\tilde{\mathcal{I}}_P^F &= \left(\frac{\mathcal{C}_s^e}{\tilde{\mathcal{C}}_s}\right)^2\frac{1-\nu_e^2\tilde{\nu}_s+\frac{\alpha(2+\alpha)}{2}(1+\nu_e\tilde{\nu}_s)}{1-\nu_e^2+\frac{\alpha(2+\alpha)}{2}(1+\nu_e)}-1, && \text{(B.25)}\\
\tilde{\mathcal{I}}_\sigma^F &= \left(\frac{\mathcal{C}_s^e}{\tilde{\mathcal{C}}_s}\right)^2\left(\tilde{\nu}_s-1\right), && \text{(B.26)}\\
\tilde{\mathcal{I}}_P^S &= \tilde{\nu}_s-1+\tilde{\nu}_s\frac{\mathcal{C}_s^{e2}-\tilde{\mathcal{C}}_s^2}{\tilde{\mathcal{C}}_s^2}, && \text{(B.27)}\\
\tilde{\mathcal{I}}_\sigma^S &= \frac{\mathcal{C}_s^{e2}-\tilde{\mathcal{C}}_s^2}{\tilde{\mathcal{C}}_s^2}. && \text{(B.28)}
\end{aligned}$$

Appendix C. Dimensionless formulation of Keramat et al.'s model

The model of Keramat et al. [28] reads

$$\begin{aligned}
\partial_t W^* &= -\partial_z P^*, && \text{(C.1)}\\
\partial_t P^*+\partial_z W^*-2\nu_e\partial_z\dot{\zeta}^* &= \frac{2\left({\nu_e}^2-1\right)}{\alpha}\partial_t\int_0^t\mathcal{I}_{ker}^*(t')P^*(t-t')dt', && \text{(C.2)}\\
\partial_\tau\sigma_{zz}^*-\frac{\nu_e}{\alpha}\partial_\tau P^*-\rho_s c_s^{e2}\partial_z\dot{\zeta}^* &= -\rho_s c_s^{e2}\partial_t\int_0^t\mathcal{I}_{ker}^*(t')\sigma_{zz}^*(t-t')dt'+\frac{\nu_e}{\alpha}\partial_t\int_0^t\mathcal{I}_{ker}^*(t')P^*(t-t')dt', && \text{(C.3)}\\
\rho_s\partial_\tau\dot{\zeta}^*-\partial_z\sigma_{zz}^* &= 0, && \text{(C.4)}
\end{aligned}$$

where the original hydraulic head H terms have been substituted by the pressure $P = \rho_f g H$, and

$$\mathcal{I}^*_{ker} = \frac{d}{dt} J^*(t), \tag{C.5}$$

the time derivative of the [28]'s Fourier creep function. The equations set (C.1)-(C.4) are now regarded under dimensionless form according to the scaling provided from (19) to (22) and by assuming the creep function to scale as the inverse of the elastic Young modulus, i.e. $J^*(t) = J(\tau)/E_e$. It then yields

$$\partial_t \int_0^t \mathcal{I}^*_{ker}(t^{'}) P^*(t - t^{'}) dt^{'} = \frac{\mathcal{D}}{\mathcal{C}_s^{e2}} \frac{W_0}{L} \partial_\tau \int_0^\tau \mathcal{I}_{ker}(\tau^{'}) P(\tau - \tau^{'}) d\tau^{'}, \tag{C.6}$$

$$\partial_t \int_0^t \mathcal{I}^*_{ker}(t^{'}) \sigma^*_{zz}(t - t^{'}) dt^{'} = \frac{\mathcal{D}}{\mathcal{C}_s^{e2}} \frac{W_0}{L} \partial_\tau \int_0^\tau \mathcal{I}_{ker}(\tau^{'}) \sigma_{zz}(\tau - \tau^{'}) d\tau^{'}, \tag{C.7}$$

so that

$$\partial_\tau W = -\partial_Z P, \tag{C.8}$$

$$\partial_\tau P + \partial_Z W - 2\alpha\nu_e \partial_Z \dot{\zeta} = \frac{2\mathcal{D}\left({\nu_e}^2 - 1\right)}{\alpha \mathcal{C}_s^{e2}} \partial_\tau \int_0^\tau \mathcal{I}_{ker}(\tau^{'}) P(\tau - \tau^{'}) d\tau^{'}, \tag{C.9}$$

$$\partial_\tau \sigma_{zz} - \frac{\nu_e}{\alpha} \partial_\tau P - \frac{\alpha \mathcal{C}_s^{e2}}{\mathcal{D}} \partial_z \dot{\zeta} = -\partial_\tau \int_0^\tau \mathcal{I}_{ker}(\tau^{'}) \sigma_{zz}(\tau - \tau^{'}) d\tau^{'} + \frac{\nu_e}{\alpha} \partial_\tau \int_0^\tau \mathcal{I}_{ker}(\tau^{'}) P(\tau - \tau^{'}) d\tau^{'}, \tag{C.10}$$

$$\frac{\alpha}{\mathcal{D}} \partial_\tau \dot{\zeta} - \partial_Z \sigma_{zz} = 0. \tag{C.11}$$

Finally, in the frequency-domain (C.8)-(C.11) achieve as follows

$$i\omega \tilde{W} = -\partial_Z \tilde{P}, \tag{C.12}$$

$$i\omega \tilde{P} + \partial_Z \tilde{W} - 2i\omega\alpha\nu_e \partial_Z \tilde{\zeta} = -\frac{2\mathcal{D}\left(1 - \nu_e^2\right)}{\alpha \mathcal{C}_s^{e2}} i\omega \tilde{\mathcal{I}}_{ker}(\omega) \tilde{P}(\omega), \tag{C.13}$$

$$i\omega \tilde{\sigma}_{zz} - \frac{\nu_e}{\alpha} i\omega \tilde{P} - \frac{\alpha \mathcal{C}_s^{e2}}{\mathcal{D}} \partial_z \tilde{\zeta} = -i\omega \tilde{\mathcal{I}}_{ker}(\omega) \tilde{\sigma}_{zz}(\omega) + \frac{\nu_e}{\alpha} i\omega \tilde{\mathcal{I}}_{ker}(\omega) \tilde{P}(\omega), \tag{C.14}$$

$$\frac{\alpha}{\mathcal{D}} \omega^2 \tilde{\zeta} + \partial_Z \tilde{\sigma}_{zz} = 0, \tag{C.15}$$

which is equal to (88)-(91).

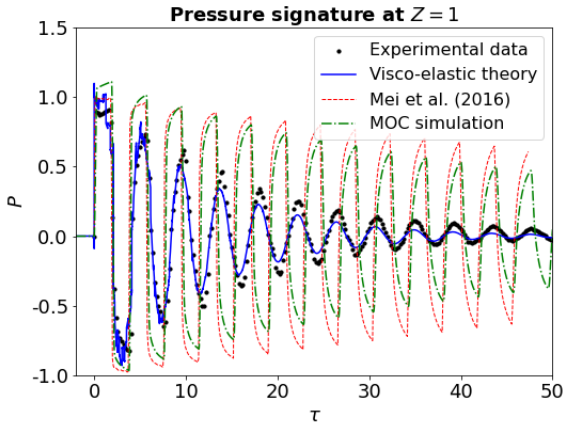

(a) Time-dependent pressure signature at the valve compared to the non-FSI Mei and Jing [16]'s theory.

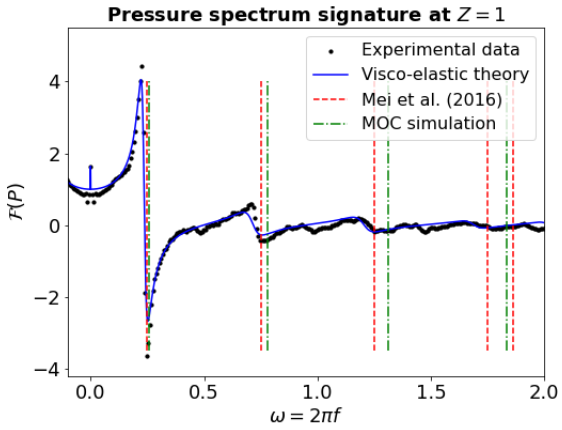

(b) Positive-half pressure signal spectrum at the valve.

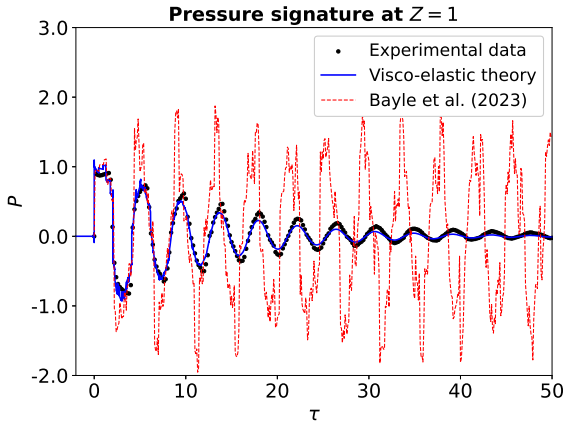

(c) Time-dependent pressure signal at the valve compared to the FSI, fluid non-viscous Bayle and Plouraboué [35]'s theory.

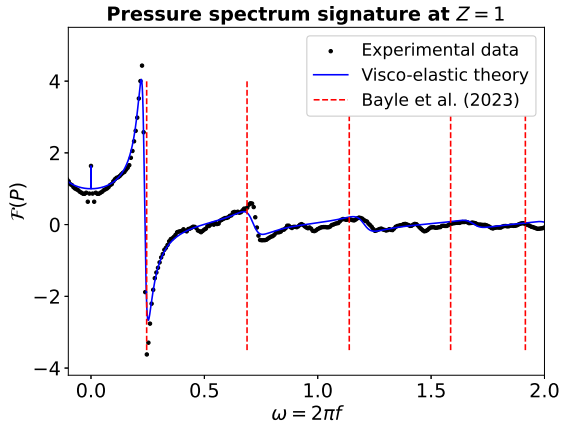

(d) Positive-half pressure signal spectrum at the valve. The Bayle and Plouraboué [35]'s resonant frequencies are depicted by dotted red lines.

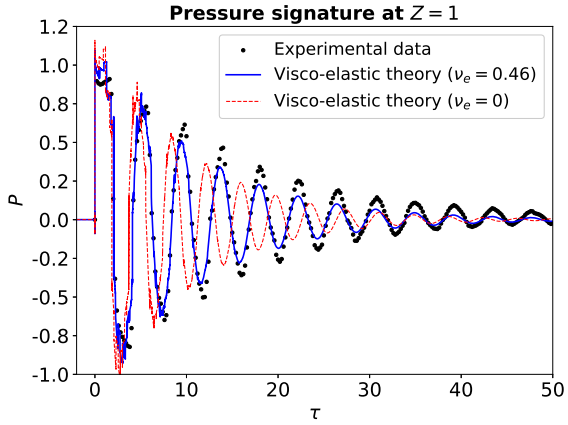

(e) Limit in $\nu_e \to 0$ of the visco-elastic solution.

Figure 2: Dimensionless time (using (4)) and frequency (using (6)) pressure signature at the valve comparing model's prediction with the experiment of Pezinga et al., [33]. The elastic signature is also depicted to point-out (a) the fluid viscous damping without FSI in the elastic pipe (b) the associated resonant frequencies (Mei and Jing [16]'s resonant frequencies are depicted by dotted red lines. Numerical MOC resonant frequencies with a viscous damping model (Darcy-Weisbach+Zielke's one) are provided in dotted green vertical lines) (c) the elastic FSI effects without fluid viscous damping (d) the associated resonant frequencies. Figure (e) displays the limit $\nu_e \to 0$ of (83)'s IFFT compared to Pezinga et al. [33]'s experiment.

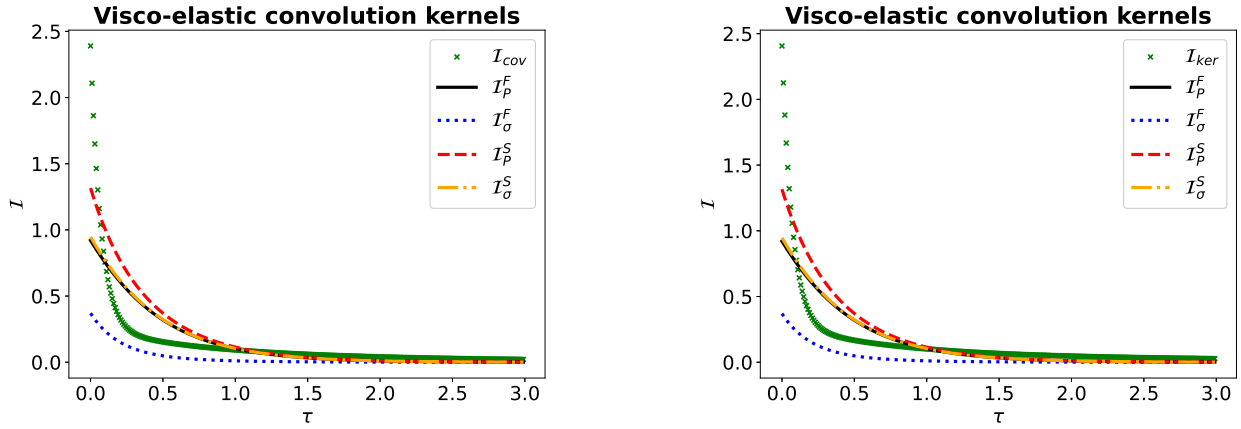

(a) (b)

Figure 3: Comparison to (a) Covas et al. [13]'s and (b) Keramat et al. [28]'s visco-elastic convolution kernels for the experimental data of Covas et al. [19, 13]. Dimensionless time τ (using (4)) has been used.

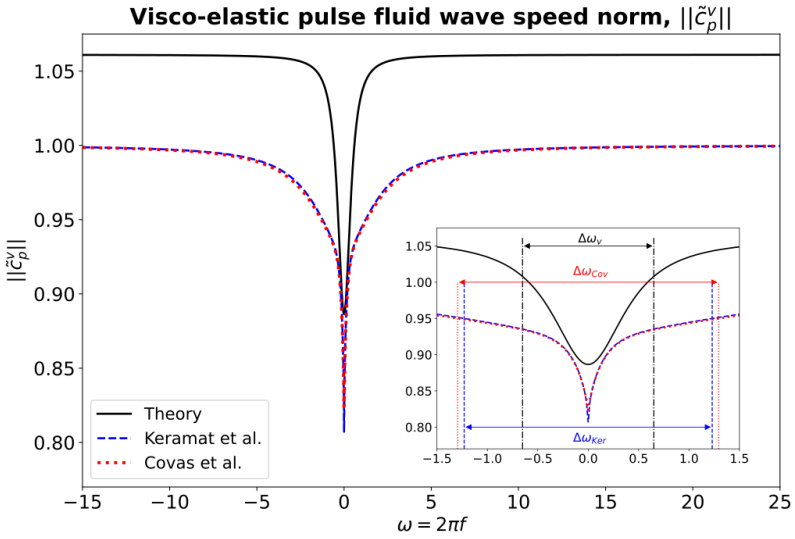

(a)

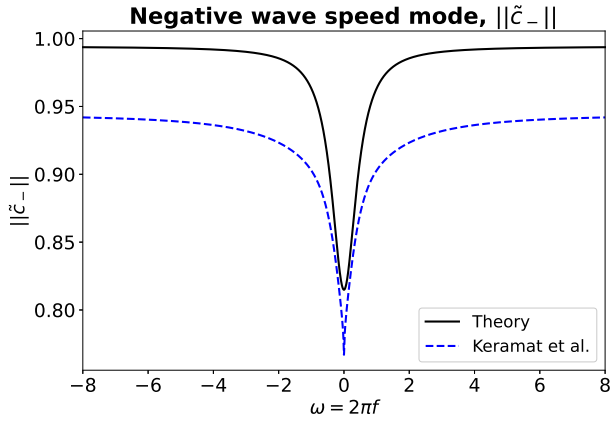

(b)

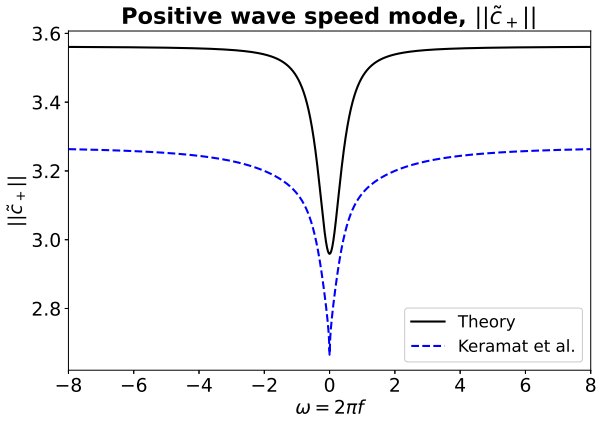

(c)

Figure 4: Comparison of frequency domain dependence of dimensionless visco-elastic velocities obtained from fitting parameters to the experimental data of [19, 13]. (a) $\tilde{c}_p^v(\omega)$ (49), (b) $\tilde{c}_+$ (53), (c) $\tilde{c}_-$ (53). Dimensionless pulsation ω using (6) have been used.

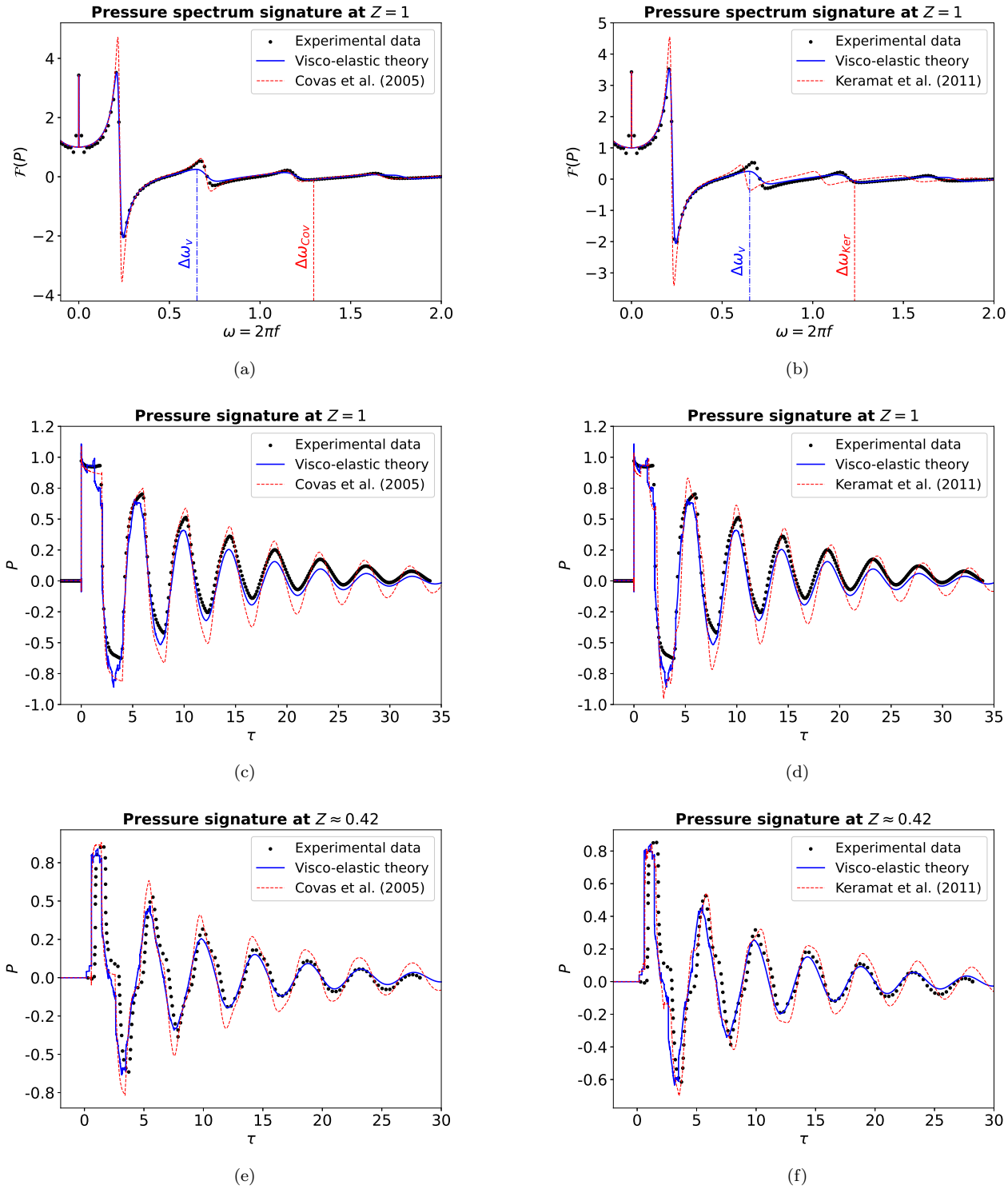

Figure 5: Comparison between the proposed rheology-based model and [13] and [28] ones for the pressure signal at various location for the reservoir-pipe-anchored valve configuration. Dimensionless pulsation ω using (6) have been used in (a) and (b), dimensionless time using (4) in (c), (d), (e) and (f).

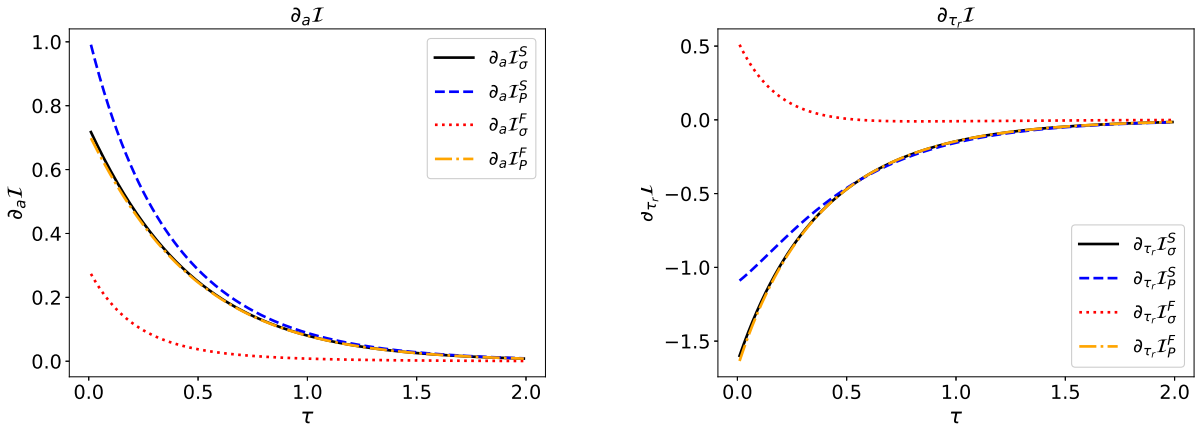

(a) (b)

Figure 6: Dispersive behaviour of the visco-elastic corrective pulse wave speed, $\tilde{c}_p^v$ versus dimensionless time (using (4)).

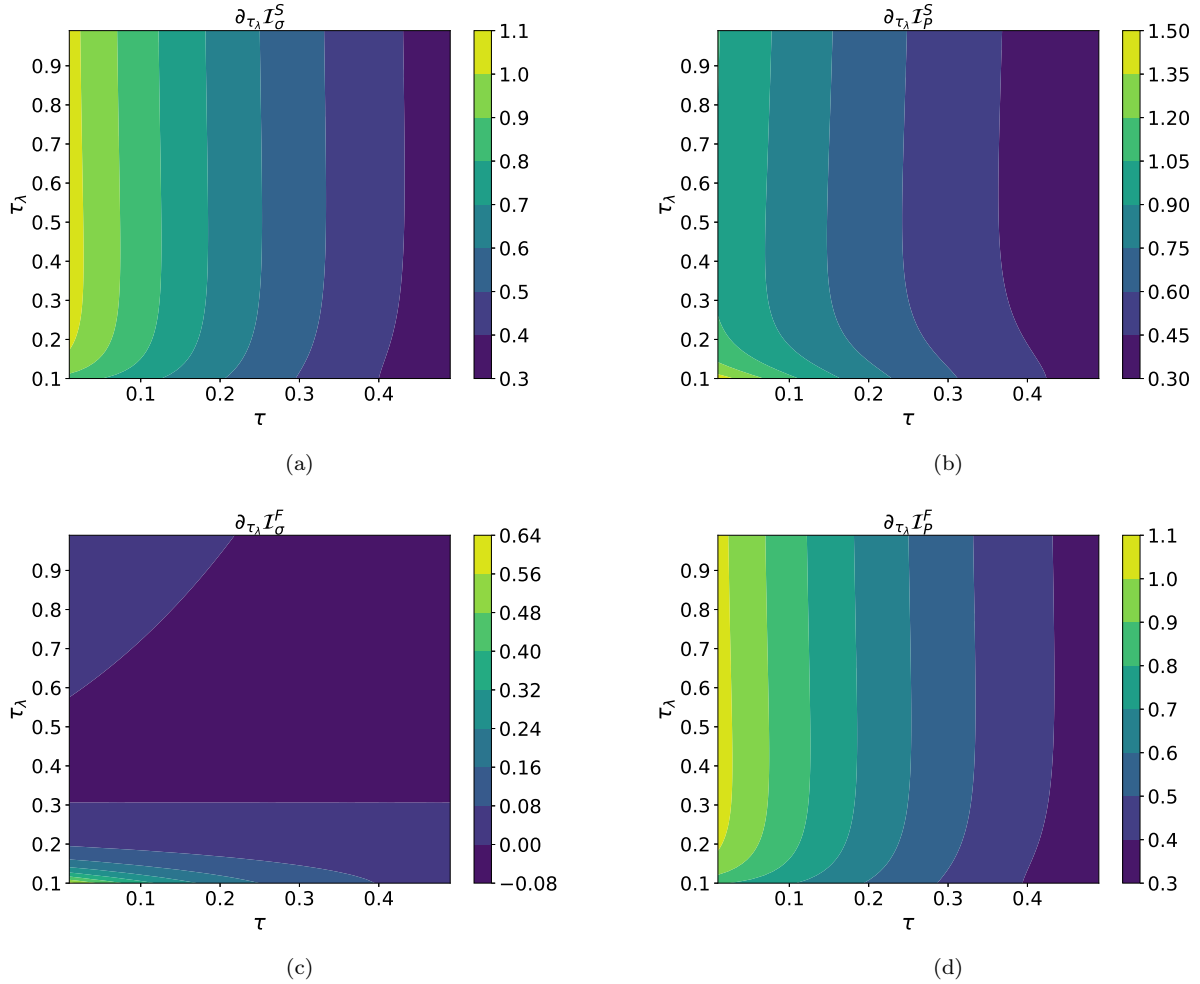

(a) (b) (c) (d)

Figure 7: Visco-elastic kernels derivatives with respect to parameter τ_λ versus dimensionless time (using (4)).

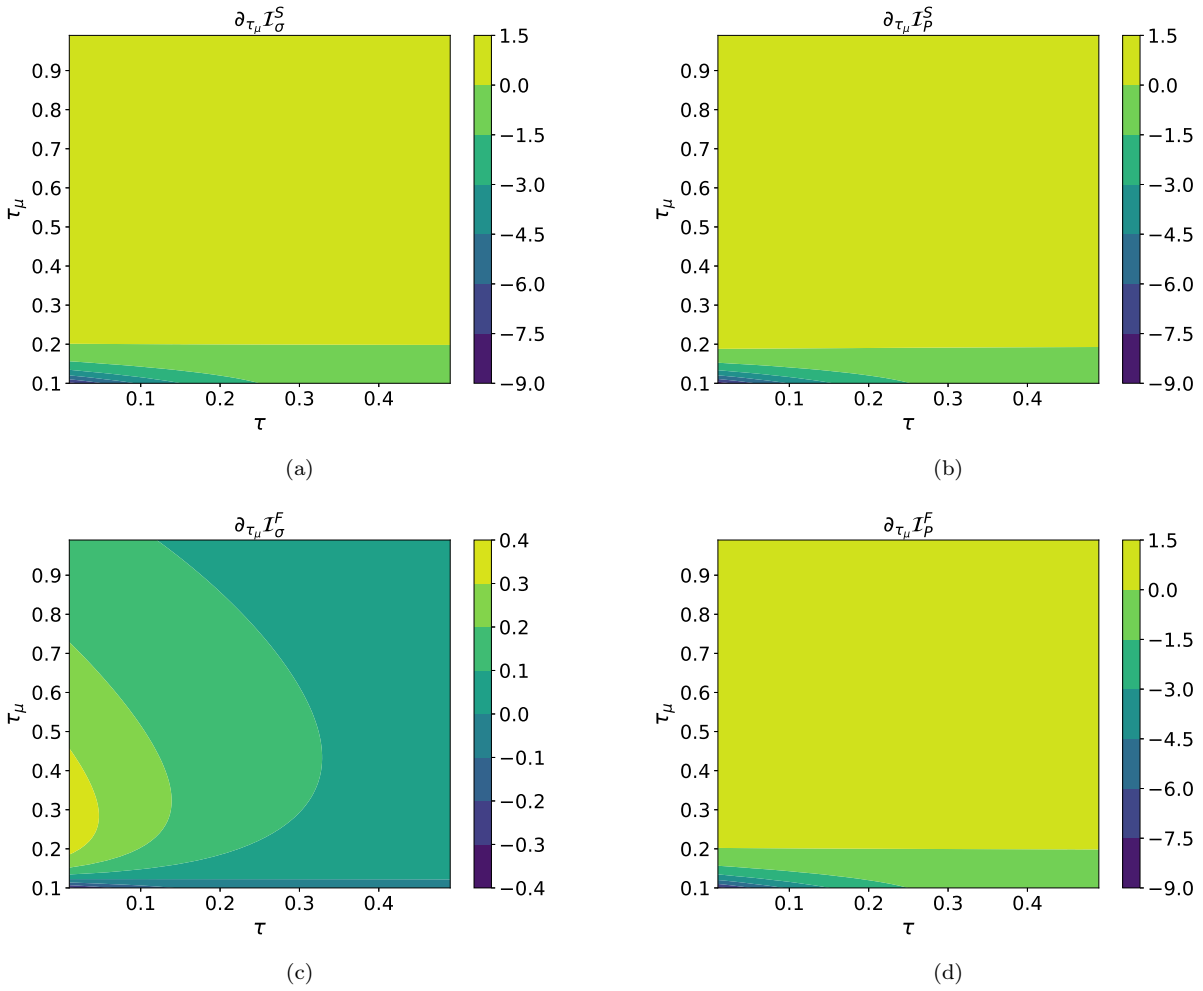

Figure 8: Visco-elastic kernels derivatives with respect to τ_μ versus dimensionless time (using (4)).

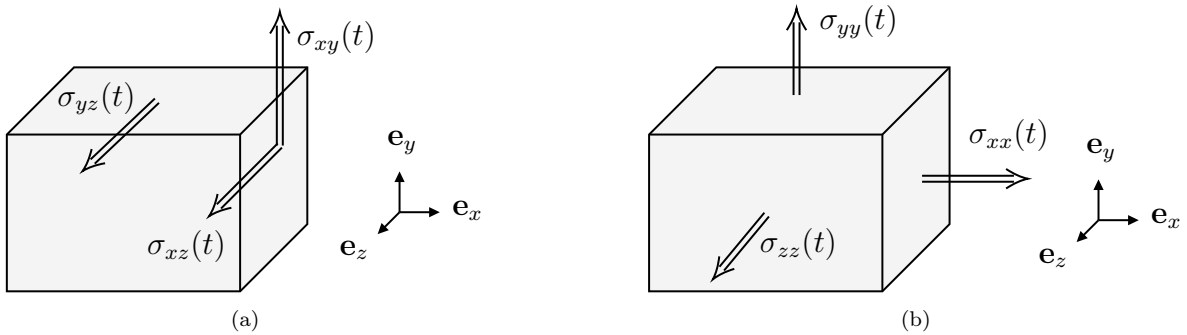

Figure A.9: Sketch of (a) shear, and (b) creep applied mechanical stress configurations on a visco-elastic material.

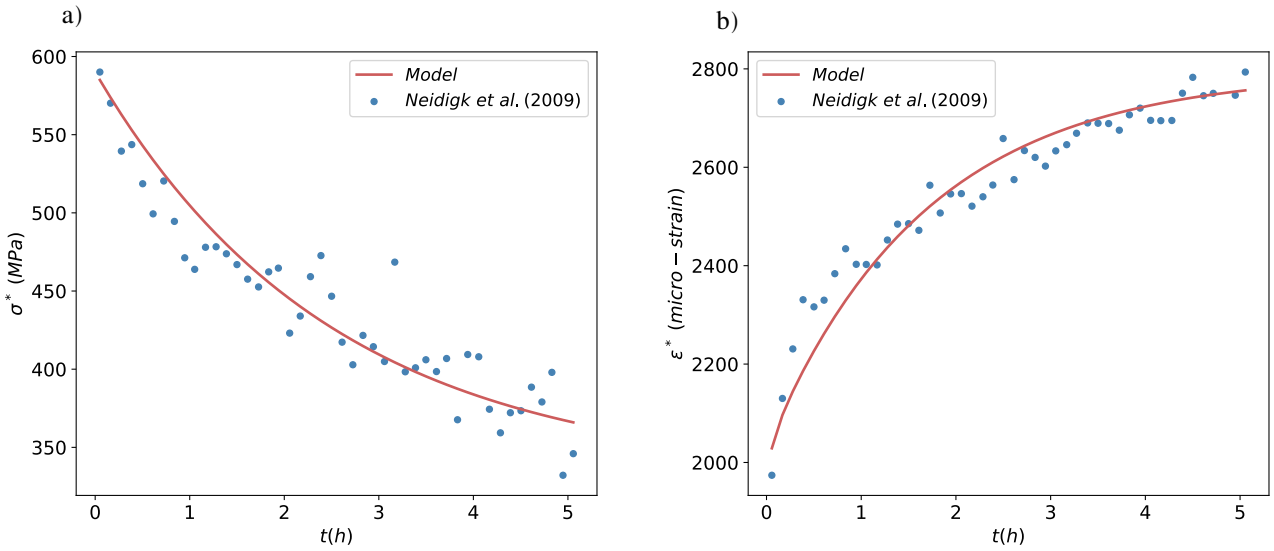

Figure A.10: Plot of the stress (a) and strain (b) evolution with time based on the femur bones media.